Ultraviolet-Visible Diffuse Reflectance Spectroscopy (UV-Vis DRS), a rapid and non-destructive analytical tool for the identification of Saharan dust events in Particulate Matter filters

TITLE

Ultraviolet-Visible Diffuse Reflectance Spectroscopy (UV-Vis DRS), a rapid and non-destructive analytical tool for the identification of Saharan dust events in Particulate Matter filters

AUTHORS

Pietro Morozzi [a]

Barbara Ballarin [b]

Erika Brattich [c]

Franco Lucarelli [d]

Silvia Nava [d]

Pedro J. Gómez-Cascales [e]

Jose A. G. Orza [e]

Laura Tositti [a]

[a] Department of Chemistry "G. Ciamician", University of Bologna, Via Selmi, 2, 40126 Bologna, Italy

[b] Department of Industrial Chemistry Toso Montanari, University of Bologna, Viale del Risorgimento, 4, 40136 Bologna, Italy

[c] Department of Physics and Astronomy, University of Bologna, Via Irnerio, 46, 40126 Bologna, Italy

[d] Department of Physics and Astronomy, University of Florence and National Institute of Nuclear Physics (INFN), Florence Section, Via Sansone, 1, 50019 Sesto Fiorentino, Italy

[e] SCOLAb, Department of Applied Physics, University Miguel Hernandez de Elche, 03202 Elche, Spain

***Corresponding author:** Pietro Morozzi

e-mail address: pietro.morozzi2@unibo.it

mailing address: Via Selmi 2, 40126 Bologna (ITALY)

ABSTRACT

Mineral dust represents one of the main components of particulate matter (PM) in the Mediterranean area. The rapid identification of Saharan dust events in PM samples is desirable and required for several reasons, including their role in direct effect on climate by radiative forcing as well as their adverse effects on human health.

For this purpose, the feasibility of UV-Vis Diffuse Reflectance Spectroscopy (UV-Vis DRS) is described as a rapid, inexpensive and non-destructive method of analysis of PM filters. The method developed allows to parameterize the PM filter colors and to obtain semi-quantitative data related to iron oxide minerals, mainly hematite and goethite, two of the most representative minerals of Saharan dust in the Mediterranean area. The obtained results were validated based on the correlation between the spectrophotometric data of iron oxides from the membranes with the quantitative assessment of the concentration of iron by Particle Induced X-ray Emission (PIXE). Moreover, colorimetric parameterization allows setting up a classification approach for filters with potential for a posteriori use of this data in the study of the optical behavior of aerosol particles in the air.

In this work, it is demonstrated how, as the concentration of iron mineral oxides and especially of hematite increases, the extent of redness color in PM filters grows up. Therefore, this technique can be extremely useful for a rapid, cheap and unambiguous identification of Saharan dust events in PM filters. The diagnosis of Saharan dust events was performed on PM_{10} filters with a strong mineral dust component and demonstrated with the residence time analysis of back-trajectory ensembles, proving the reliability of this non-destructive methodology.

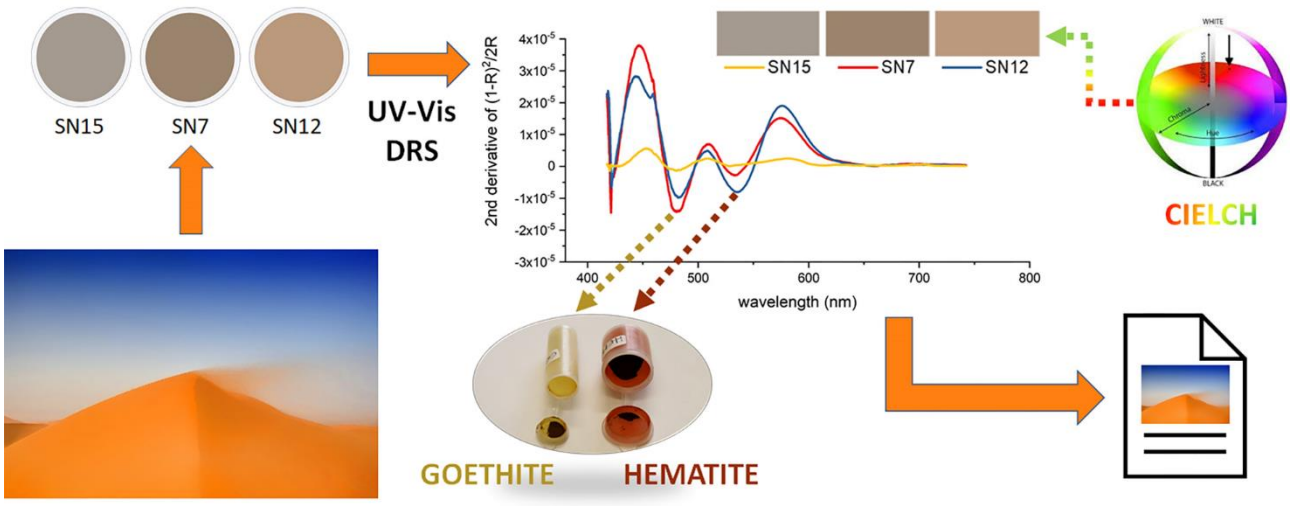

KEYWORDS

Saharan dust, diffuse reflectance spectroscopy, iron oxide minerals, colorimetry, chemometrics, residence time analysis

HIGHLIGHTS

- Rapid and non-destructive technique for particulate matter filter analysis
- Quick identification of filter colour
- Semi-quantitative analysis of iron oxide minerals
- Fast detection of Saharan dust events
- Determination of particular events and/or emission sources of particulate matter

1. INTRODUCTION

Mineral dust uplifted into the atmosphere by the wind in arid and semi-arid regions of North Africa are often transported across thousands of kilometers including both the northernmost European territory and/or the American continent (e.g., Middleton & Goudie, 2002). Overall the Mediterranean basin owing to proximity and average circulation patterns, is directly and widely affected by these phenomena throughout the year with events whose intensity and frequency are object of extensive research (Brattich et al., 2015a; Brattich et al., 2015b; Cabello et al., 2016; Cuevas et al., 2017; Cusack et al., 2012; Israelevich et al., 2012; Riccio et al., 2009; Tositti et al., 2014). The frequency and intensity of Saharan Dust outbreaks are presently reported as increasing due to the effect of global warming (Middleton & Goudie, 2002; Soleimani et al., 2020). These events can contribute to an increase of PM_{10} levels above the limits allowed by the air quality regulations drawing attention on health threatens as well as on their correct management (Diapouli et al., 2017; Krasnov et al., 2014; Matassoni et al., 2011; Nava et al., 2012; Querol et al., 2019). In particular, the European Air Quality Directive 2008/50/EC establishes that PM_{10} (i.e. PM with an aerodynamic diameter less than 10 μm) daily mean value may not exceed 50 $\mu g/m^3$ more than 35 times in a year and that the PM_{10} annual mean value may not exceed 40 $\mu g/m^3$ (EU, 2008). similarly, the World Health Organization (WHO) recommends a PM_{10} daily mean value less than 50 $\mu g/m^3$ but with a considerably lower PM_{10} annual mean value of 20 $\mu g/m^3$ (WHO, 2006). The European legislation allows subtracting the contribution associated to natural episodes and therefore the quantification of the African dust contribution is

85 relevant in the air quality field (EEA, 2012). The relevance of this quantification is not limited to
86 legislation, however.

87 Saharan dust plays a significant role in the climate system by affecting the radiative balance of the
88 planet. Dust particles heavily modify the optical properties of the troposphere by the so-called direct
89 effect (e.g., Chin et al., 2009; Ginoux, 2017; IDSO, 1981; Littmann & Steinrücke, 1989; Sokolik &
90 Toon, 1999), while recent research has shown it plays also a fundamental role in cloud processing
91 and nucleation, i.e. by indirect effect (see for example Reicher et al., 2019). Furthermore, mineral
92 dust strongly influences the atmospheric reactivity through complex surface chemical reactions
93 (Usher et al., 2003). Mineral particles may also affect the oxidant capacity of the troposphere by
94 catalyzing ozone destruction, an important pollutant and reactive greenhouse gas (Bonasoni et al.,
95 2003; Dickerson et al., 1997; Prospero et al., 1995). Moreover, iron contained in Saharan dust plumes
96 can settle on oceanic surfaces and be a nutrient for marine phytoplankton, with beneficial results for
97 oligotrophic aquatic systems but potentially damaging the eutrophic ones (e.g., Bristow et al., 2010;
98 Molinaroli & Masiol, 2006). However, Saharan dust has been often associated with a coral decline in
99 the Caribbean region, suggesting that either mineral or microbiological components of Saharan dust
100 may reveal detrimental to especially fragile ecosystems (Garrison et al., 2003; Shinn et al., 2000).
101 This is in agreement with further, not negligible, implications linking Saharan dust transport with an
102 increase in the mortality rate and adverse health effects on the Mediterranean population (Karanasiou
103 et al., 2012; Querol et al., 2019; Stafoggia et al., 2016).

104 Common procedures to identify dust outbreaks use a combination of back-trajectory analysis, satellite
105 retrievals, and the output of dust prediction models. Collectively they provide a reasonable degree of
106 evidence though each of these tools has limitations: a back-trajectory travelling over North Africa is
107 not always associated to dust advection; satellite retrievals are limited by cloud coverage and transit
108 time; uncertainties in dust model estimates remain, due to incomplete representation of several
109 processes. All of this information is frequently combined with PM_{10} levels or columnar aerosol

properties at the study site. These levels are compared with local threshold values or background levels obtained by their own time series (Barnaba et al., 2017) or with PM_{10} concentrations at a close regional background site (EC Commission, 2011; Escudero et al., 2007). Saharan mineral dust consists mainly of silicates, aluminum oxides, carbonates, gypsum, and iron oxides, with a specific composition that depends on the geological material from its lifting place (e.g., Linke et al., 2006). Chemical speciation analysis is largely used to characterize aerosol composition as a function of its sources. Mineral dust is successfully identified with all the basic techniques devoted to elemental inorganic analysis; X-ray emission techniques such as Particle Induced X-ray Emission (PIXE) and X-ray fluorescence (XRF) are the most efficient and non-destructive ones since they allow a prompt detection of the abundant geochemical components, without any demanding and costly chemical processing in advance. Crustal elements like silicon (Si), aluminum (Al), titanium (Ti), calcium (Ca), and iron (Fe) are successfully used to identify Saharan dust events, as reported by, e.g., Alastuey et al., 2016; Formenti et al., 2010; Marconi et al., 2014; Nava et al., 2012; Rodríguez et al., 2020. In most cases, elemental analysis is complemented by ion chromatography wherein the most informative species associated with mineral dust is calcium ion (Ca^{2+}) (Escudero et al., 2005; Flentje et al., 2015; Putaud et al., 2004). This approach can be integrated by the detection of mineral species such as quartz, feldspars, illite, smectite, kaolinite, chlorite, vermiculite, mica, calcite, gypsum, hematite and goethite (Caquineau et al., 2002; Journet et al., 2014) requiring X-Ray Diffraction (XRD) (Menéndez et al., 2007; Shao et al., 2007), and Scanning Electron Microscopy (SEM) (Menéndez et al., 2007; Remoundaki et al., 2011). However, many of these analytical techniques are expensive, time consuming, and require sophisticated instrumental facilities and highly skilled personnel.

In this article, a procedure based exclusively on Ultraviolet-Visible Diffuse Reflectance Spectroscopy (UV-Vis DRS) (Torrent & Barrón, 2008) is proposed as a simple, cheap, efficient, rapid, and non-destructive analysis of particulate samples collected on a membrane for Saharan Dust transport diagnosis. This method is based on iron oxides, which account for approximately 2 to 7 % in weight

of the total amount of mineral dust (Alfaro et al., 2004; Formenti et al., 2008; Goudie et al., 2006) in atmospheric aerosol and mainly consist of goethite (predominant, 52-78% of the total iron oxides) and hematite (22-48 % of the total iron oxides) (Formenti et al., 2014; Lafon et al., 2006; Shi et al., 2012). Since these minerals are important markers of mineral dust (Formenti et al., 2014; Lafon et al., 2006; Shi et al., 2012), they can be used as proxies for Saharan dust events in locations characterized by a low background of iron oxides from other more common sources, i.e. the Earth's crust especially by soil resuspension or technogenic ones such as metal works. Hematite and goethite are typically characterized by intense colors, which can impart a yellowish to red color to atmospheric dust particles (Arimoto et al., 2002). The proposed methodology is characterized by: (a) color parametrization and (b) iron mineral oxides semi-quantification of the analyzed PM filters, followed by (c) chemometric tools. It can be integrated into routine sampling when no further speciation analysis is needed. This procedure does not intend to replace the existing speciation methods, but to support them in order to enhance and corroborate the identification of Saharan Dust transport episodes.

2. MATERIALS AND METHODS

The Materials and Methods section is organized as follows:

(a) Subsection 2.1 describes the PM_{10} samples used for the application and characterization of the UV-Vis DRS methodology reported in this work;

(b) Subsection 2.2 describes exhaustively the method used, paying particular attention to the instrumental configuration and analysis method of PM filters (subsection 2.2.1), how it is possible to parameterize the colour of the analyzed filters (subsection 2.2.2) and obtain semi-quantitative data of iron oxide minerals from sample reflectance spectra (subsection 2.2.3);

158 (c) Subsection 2.3 presents the validation of the proposed methodology. After checking the main
159 results of the proposed methodology (subsection 2.3.1), chemometric methods are used to identify
160 the PM filters that have been subjected to a Saharan dust transport event (subsection 2.3.2.1), and the
161 diagnosis obtained are assessed and confirmed by a residence time analysis of back-trajectory
162 ensembles (subsection 2.3.2.2).

163 **2.1 Particulate matter samples**

164 PM_{10} samples analyzed in this work were collected at Sierra Nevada a high altitude site (37.096 N, -
165 3.387 W, 2550 m a.s.l.) in Southern Spain, within the framework of the Spanish national project
166 FRESA (Impact of dust-laden African air masses and of stratospheric air masses in the Iberian
167 Peninsula. Role of the Atlas Mountains, Ref: CGL2015-70741-R). The sampling station is located in
168 an area scarcely influenced by traffic and other anthropogenic sources, but strongly impacted by
169 Saharan dust incursion events due to its proximity to North Africa (Figure 1).

170 PM sampling was carried out using a high volume PM_{10} sampler (CAV-A/mb, MCV S.A.) on a
171 weekly basis (168 h at 30 m^3/h) using quartz filters (Ø 15 cm, Whatman QM-A quartz filters) from 8
172 June to 11 October 2016. Nineteen weekly PM_{10} samples (labeled as SN1-SN19) were overall
173 obtained and processed along with three field blanks (labeled as B1-B3).

174 **2.2 The UV-Vis DRS methodology**

175 *2.2.1 Sample preparation and UV-Vis DRS analysis*

176 UV-Vis Diffuse Reflectance Spectroscopy is a widely used, basic spectrophotometric technique for
177 the analysis of powders and surfaces, requiring a negligible sample preparation (Torrent & Barrón,
178 2008). It is based on the surface dispersion of a fraction of the UV-Vis incident radiation on it. A UV-
179 Vis collimated light beam is directed with a certain angle onto the sample and, as a result, an ensemble
180 of optical processes leads to radiation reflection by the sample surface on the whole overlying

hemisphere. Generally, the radiation reflected by a sample can be considered as the sum of two components: regular (or specular) and diffuse (or nondirectional) reflectance (e.g., Torrent & Barrón, 2008). Regular reflectance occurs when incident radiation hits an ideally smooth and planar surface (i.e. without roughness) of the sample, and it is then reflected at an angle equal to the angle of incidence (Fresnel law). Instead, diffuse reflectance is a combination of several optical phenomena, such as multiple reflections, scattering and refraction, which disperse the radiation at all of the angles of the hemisphere of origin of the incident radiation (Blitz, 1998). Diffuse reflectance is the most informative component as it regards the physico-chemical properties and color of the surface (Sellitto et al., 2008).

Diffuse reflectance spectroscopy of PM filters is conducted with an ordinary UV-Vis spectrophotometer (in this work, a Perkin Elmer Lambda 35 UV-Vis Spectrophotometer was used) equipped with a suitable accessory, known as integrating sphere, which allows the measurement of all the reflection produced by the sample, which is diffused in the inner walls of the integrating sphere. The analysis does not include any sample chemical preparation: to the scope a squared sample portion of 1.8 cm x 1.8 cm is placed inside a flat sample holder, designed to position the sample for beam irradiation at a 0° incidence angle, and lodged over the reflectance sample port of the integrating sphere, a 50 mm diameter Labsphere RSA-PE-20 (Labsphere, United States). With the 0° sample holder in place, any specular component of reflection from the sample is excluded from measurement, since this component is directed out of the sphere through the transmittance sample entrance port. This integrating sphere configuration is named 0°/diffuse (0°/d) and Figure 2 shows its operating scheme. Square sample pieces were carefully cut by means of a square die-cutting tool with a side of 1.8 cm. The UV-Vis DRS analysis of the latter is non-destructive since the side containing the particulate material is analyzed as it is, without any treatment and contact with the instrument. Firstly, a Spectralon white standard (USRS-99-010-EPV, Labsphere, United States) was analyzed as a reference and the instrumental autozero was performed. Then, one aliquot from each field blanks (B1-

B3) was prepared and B1 portion was used for the background correction. Subsequently, the analysis of the remaining blank portions (B2 and B3) and the PM sampled filters was carried out. In particular, in addition to the two blank portions, three different portions of each PM sampled filter were prepared and analyzed in order to compute average values and standard deviations of each sample outcome and, therefore, account for possible filter anisotropy. In this way, a total of 59 analyses were completed for this work. Therefore, the percentage reflectance (% R), i.e. the ratio between the intensity of the radiation reflected by the sample and the intensity of the total radiation reflected by a white diffuse reflectance standard, was determined for each of the analyzed portions. In particular, this parameter was measured as a function of the wavelength λ of the UV-Vis incident radiation (i.e., reflectance spectra were obtained), based on the following instrumental parameters: λ range = 780 - 380 nm; resolution = 0.3 nm; scan speed = 480 nm/min, smoothing = 2 nm, and slit = 2 nm.

2.2.2 Color parametrization

Sample color can be obtained by its UV-Vis reflectance spectrum. Indeed, sample color strongly depends on its diffuse reflection: an object irradiated by a light source disperses part of the incident radiation by diffuse reflection, which is subsequently collected by the eyes of an observer which in turn act as transducers, converting the light signal into appropriate electrical impulses for the brain. Ultimately, these impulses are integrated and processed by the latter, which generates the color perception for the observer (Kremers et al., 2016). Therefore, color is an extremely complex and subjective entity, as it is not a specific feature of the object itself but depends on many variables such as the light source, the optical behavior of the object, the observer's eyes and brain, etc. Since 1931, the International Commission on Illumination (CIE) has outlined guidelines to standardize color perception, through the standard definition of three elements: light sources, observers, and colorimetric spaces. The latter are mathematical models able to define the color of an object in a rigorous manner (Ibraheem et al., 2012). One of the currently most used colorimetric space is the CIE L*a*b* (CIELAB) (ISO-CIE 11664-4-2019), which uses three cartesian components to uniquely

define color sample: L^*, that indicates the CIELAB lightness in the range 0 (pure black) to 100 (pure white); a*, that indicates the CIELAB redness-greenness coordinate; and b*, that indicates the CIELAB yellowness-blueness coordinate. This colorimetric space can also be defined in polar coordinates, thus obtaining the CIE $L^*C_{ab}{}^*h_{ab}°$ space (CIELCH) (ISO-CIE 11664-4-2019), wherein: L^* always indicates the CIELAB lightness; $C_{ab}{}^*$ represents the CIELAB chroma, a measure of the color intensity, defining how much a certain color shade is "contaminated" by gray; and $h_{ab}°$ indicates the CIELAB hue angle, whose value is expressed in degrees and describes the color tone. In particular, the 0° angle represents the red color. Because of their easy interpretability, in this work the mathematical definition of the colors of the analyzed portion samples was carried out employing the CIELAB and CIELCH spaces, starting from the reflectance spectra obtained and using the Color 2.01 software (Perkin Elmer Ltd, United Kingdom). Standard Illuminant D65 was set up as a representation of solar light source, according to CIE (ISO-CIE 11664-2-2020), and an observer angle of 10° was set up because provide the best average spectral response in human observers (ISO-CIE 11664-1-2019). Average values and the standard deviations of the colorimetric parameters (L^*, a^*, b^*, $C_{ab}{}^*$, and $h_{ab}°$) were calculated for the blank filter (B) and the 19 samples (SN1,…SN19) starting from the analyzed portions for each sample. The CIELAB average data were used for color visualization through the online tool nix Color Sensor (https://www.nixsensor.com/free-color-converter/). In this step, illuminant and reference (observer) angle have been set as D65 and 10°, respectively.

2.2.3 Semi-quantification of iron oxide minerals

Diffuse reflectance measurements are extremely useful for the individuation and quantification of the most important sample pigments. Indeed, they exhibit attenuation in reflectance spectra due to their light-absorption in specific UV-Vis wavelength ranges. Iron oxide minerals absorption is associated with their electronic transitions within the $3d^5$ shell of Fe^{3+} ion triggered by UV-Vis radiation (Scheinost et al., 1998) and, consequently, reflectance spectra can be useful for the assessment of these mineral species. While past work on PM membranes was mainly based on the first derivative

of the UV-Vis reflectance (e.g., Arimoto et al., 2002; Shen et al., 2006), in this work we compute the second derivative of the Kubelka-Munk (K-M) function spectra. This method has been widely used for the assessment of iron oxides in soil samples (Barrón & Torrent, 1986; Fernandez et al., 1992; Sellitto et al., 2009; Szalai et al., 2013) and less frequently for PM filters analysis (Lafon et al., 2006), while the approach was used in several spectrophotometric applications for the most absorbing aerosol component, i.e. soot (see for example Pandey et al., 2019; Petzold et al., 2004). The calculation of the second derivative was performed using the Savitzky-Golay filter (Schafer, 2011), an averaging algorithm that fits a polynomial to the data points and allows the calculation of a derivative of this function. It was computed choosing a polynomial order of 4, i.e. using a fourth-degree equation fit of the data points and a number of smoothing points equal to 251. Processed spectra thus obtained clearly presents significant peaks due to the absorption of iron oxide minerals. The semi-quantitative data of iron oxide minerals are represented by the heights of these peaks, which were determined by tracing the "baselines", subtracting them from the starting spectrum, and quantifying the height of the resulting peak.

The conversion of the reflectance spectra into K-M spectra was carried out using the UV WinLab 2.85 Software (Perkin Elmer Ltd, United Kingdom), while the calculation of the Savitzky-Golay second derivative was performed by the software The Unscrambler V10.4 (Camo, Oslo, Norway), and the quantification of peak heights was carried out using the Peak Analyzer tool of the OriginPro 2018 software (Northampton, USA).

2.3 Validation of the methodology

2.3.1 Validation of UV-Vis DRS results

Sample color (subsection 2.2.2) was numerically defined by means of colorimetric parameters described by CIE, and semi-quantitative information about iron oxide minerals (subsection 2.2.3) were achieved by a suitable mathematical treatment of reflectance spectra. In order to validate the

semi-quantitative data of iron oxide minerals, they were compared with elemental iron concentration data (µg cm^{-2}) obtained by Proton Induced X-ray Emission (PIXE) carried out on the same PM_{10} filters using a Tandetron 3 MeV accelerator located at LABEC laboratory (Laboratorio di tecniche nucleari per l'Ambiente e i Beni Culturali, https://www.ionbeamcenters.eu/RADIATE-project-partners/infn/) of the INFN Section of Florence (Italy) (Lucarelli et al., 2014; Lucarelli et al., 2018). Since the membranes used in this work are made of quartz instead of the typical teflon (PTFE) or cellulose/nuclepore, more suitable for the PIXE technique, PIXE analysis required appropriate spectral processing owing to the huge interference of silicates in the filter medium itself as described in detail by Calzolai et al., 2006; Chiari et al., 2018; and Lucarelli et al., 2011. In brief, PM_{10} samples were irradiated with a 3.0 MeV proton beam with a 5 nA current for 60 s, with no He flow, using a scanning system allowing to analyse most of the sample area and average over possible non-homogeneous deposits.

Spearman correlation ana lysis (Akoglu, 2018) was then performed between the UV-Vis DRS outcomes (color parameters and semi-quantitative data of iron oxide minerals) with elemental iron concentration calculated by PIXE and PM_{10} obtained by gravimetry, both expressed in µg cm^{-2} for dimensional consistency. This allowed assessing the relationship between these variables and the effectiveness of the spectrophotometric outcomes in identifying Saharan Dust events.

2.3.2 Diagnosis and validation of Saharan mineral dust events

2.3.2.1 Diagnosis based on PM filters

The ultimate goal of this work is to sort out quickly but safely the PM filters exposed to Saharan Dust transport events from the others.

Therefore, Ward's cluster analysis (Ward, 1963) using squared Euclidean distance was employed for the detection of two sample clusters, respectively a cluster indicating the samples subjected to Saharan dust transport events and another cluster for all the other sample cases. After standardization by

autoscaling (van den Berg et al., 2006), the colorimetric parameters of CIELCH model (subsection 2.2.2) and the semi-quantitative data of iron oxide minerals (subsection 2.2.3) were used as starting variables. The statistical analysis was carried out by means of the software Statistica V.10 (StatSoft Inc., Tulsa, USA).

The two clusters obtained were subsequently compared with PM_{10} data normalized in air sampled volume ($\mu g/m^3$) in order to associate or exclude, in a binary way, the occurrence of a Saharan dust incursion.

2.3.2.2. Back-trajectory ensembles and residence time analysis

A residence time analysis of back-trajectory ensembles (Lin, 2012; Lupu & Maenhaut, 2002; Stohl, 1998) was carried out to assess and confirm the diagnosis made by UV-Vis DRS.

Ensembles of back-trajectories were calculated using the NOAA Hybrid Single Particle Lagrangian Integrated Trajectory (HYSPLIT_4) model (Rolph et al., 2017; Stein et al., 2015). Meteorological data from the ERA-Interim reanalysis (Dee et al., 2011) was used as input for the trajectory calculations with data interpolated into a 0.5-degree grid, to make use of the 0.5-degree model terrain available in the Hysplit model, and 27 pressure levels from 1000 to 100 hPa. The ensemble is generated by offsetting the meteorological database by one grid point in the horizontal and 0.01 sigma units in the vertical, resulting in 27 back- trajectories (Draxler, 2003). 96-hour kinematic back-trajectory ensembles were calculated starting 200 m over the sampling site at 00, 06, 12, and 18 UTC in the period 8 June – 11 October 2016.

The trajectory ensembles were grouped together according to the weekly PM sampling period. After that, a residence time analysis was performed by counting the number of trajectory endpoints over five broad regions: Africa, America, Europe, Mediterranean Sea, and Atlantic Ocean for the trajectories within each sampling period. Furthermore, two additional specific areas such as Mauritania and the Atlantic Ocean at low altitude (below 800 m) were investigated. Subsequently,

the ratio between the total counts and the total number of endpoints was calculated in order to obtain percentages of residence time for each investigated area corresponding to each PM filter (Ashbaugh et al., 1985; Orza et al., 2013; Xu et al., 2006). All the trajectory calculations were performed with R (R Core Team, 2019) scripts. Further support of the occurrence of African dust events was attained with the Merged Dark Target/Deep Blue aerosol optical depth (AOD) Collection C6 product from the Moderate Resolution Imaging Spectroradiometer (MODIS) onboard the Aqua and Terra satellites.

3. RESULTS AND DISCUSSION

Results and discussion section is organized as follows:

(a) Subsection 3.1 reports the colorimetric parameters and the related digitized colours for the analyzed PM filters, highlighting and discussing their differences.
(b) Subsection 3.2 details the semi-quantitative results of iron oxide minerals, and their processing from raw reflectance spectra.
(c) Subsection 3.3 shows the correlation between the semi-quantitative data of the iron oxide minerals, the elemental iron obtained by Proton Induced X-ray Emission (PIXE) analysis, and the colorimetric parameters.
(d) Subsection 3.4 reveals the PM filters that have been subjected to a Saharan Dust transport event and the validation of this diagnosis by residence time analysis.

3.1 The color samples

For each portion of the PM filter analyzed, the color samples were obtained by the procedure described in subsection 2.2.2. The colorimetric parameters related to the CIELAB (L^*, a^*, b^*) and CIELCH (L^*, $C_{ab}{}^*$, $h_{ab}°$) models and the subsequent color obtained for the blank filter (B) and for the 19 PM samples (SN1, …SN19) are reported in Table 1.

The collected PM samples present different colors (from gray to red) as a function of the dominating aerosol source during the respective sampling time interval. In order to examine how these samples differ in color, a graphical representation based on chroma (C_{ab}^{*}) and hue ($h_{ab}°$) is shown in Figure 3. First, in Figure 3 (a), it can be observed how the blank filter (B) remarkably differs from all the others (SN1, …SN19). In fact, the B filter is characterized by a whitish color due to the absence of particulate material, while a greyish-yellowish-reddish color characterizes the sampled filters, as can be seen in the last right column of Table 1. Sampled filters in Figure 3 (b) show a defined trend: the grayest samples (like SN15) present a higher hue value and a lower chroma value than other filters while the most reddish samples (like SN12) show a higher value of chroma and a lower value of hue. Instead, the samples with intermediate values of chroma and hue (like SN7) exhibit a browner coloration than the others. This observation is in agreement with the CIELCH color definition: a lower hue value corresponds to a color tone more shifted towards red, while a higher chroma value corresponds to a more marked color intensity (compared to the gray color that occurs at chroma values close to zero). This demonstrates how the CIELCH color space adequately describes the colors of the analyzed PM filters due to their high chromaticity. In fact, the higher efficiency of the CIELCH model as compared with the CIELAB one in assessing the differences between the more chromatic colors, since C_{ab}^{*} and $h_{ab}°$ allow a better identification of the more saturated colors than a and b (Schloss et al., 2018).

3.2 Iron oxide minerals

As previously reported in subsection 2.2.3, the calculation of the second derivative of the Kubelka-Munk function spectra was performed over the DRS spectra. This operation allows to identify decreasing peaks due to light absorption by iron oxide minerals, such as akaganéite, feroxyhyte, ferrihydrite, goethite, hematite, lepidocrocite, maghemite, and schwertmannite (Sherman & Waite, 1985; Torrent & Barrón, 2002), whose characteristics are reported in Figure 4.

As reported by Scheinost et al., 1998, only the decreasing peak at around 535 nm is specific for a single mineral (hematite), while the other peaks at 420 nm and 480 nm are shared by several other iron oxides. Therefore, the semi-quantitative nature of the spectral data of iron oxide minerals can be deduced for each portion of the PM filter through an appropriate processing of their UV-Vis reflectance spectra. For the sake of brevity/conciseness, from now on graphical plots present the results for only three characteristic filters, namely SN15, SN7, and SN12 (Figure 5). The selection of the filters is not arbitrary but relies on careful considerations based on the colors determined for these filters, as previously reported in subsection 3.1.

Figure 5 (a) reports the reflectance spectra obtained from the instrumental analysis. As can be seen, these raw spectra present a characteristic baseline due to scattering of the UV-Vis radiation with tiny signal decreases. Samples SN7 and SN12 in particular present two bands at around 480 nm and 535 nm characterized by a decrease in percentage reflectance due to absorption by iron oxides (Gonçalves et al., 2012; Torrent & Barrón, 2002), a spectral feature not present in the sample SN15. Though the attenuation in the reflectance signal due to iron oxide minerals can be observed, the latter does not allow for accurate spectral quantification. The derivative spectroscopy has been widely used to: (a) correct for baseline effects in spectra to remove non-chemical effects, (b) enhance small spectral detail, and (c) resolve overlapped band (Ojeda & Rojas, 2013). Therefore, the application of derivative spectroscopy can be particularly useful to enhance these iron peaks in UV-Vis reflectance spectra of PM filters and, subsequently, obtain their relative semi-quantitative data. As from Figure 5 (b), the processed spectra present considerably more marked decreasing peaks due to iron oxides, compared to the starting reflectance spectra reported in Figure 5 (a). Furthermore, the intensities of the original curves can be seen in the derivatives in order of intensity, and this is necessary for performing quantitative analyses. As such, three principally decreasing peaks can be identified: around 420, 480 and 535 nm, respectively.

An example is reported in Figure 5 (c). The 420 nm peak was discarded as significantly affected by the instrumental spike due to the lamp shift from Vis to UV, a detail that can be noticed in Figure 5 (a) at around 380 nm. Average values and the standard deviations of the peak heights thus obtained (h_480nm and h_530 nm) were calculated for the blank filter (B) and for the 19 samples (SN1, …SN19) starting from the three analyzed portions for each sample, and were reported in Table 2.

3.3 Validation of UV-Vis DRS results

The similarity between the sample series of iron oxide minerals semi-quantitative data (h_480nm and h_535nm) and elemental iron concentration (Fe) is reported in Figure 6. Figure 6 shows a comparable trend between the semi-quantitative data of iron oxide minerals and elemental iron concentration, validating the results and confirming the usefulness of the diffuse reflectance measurements in the analysis of iron mineral oxides. Table 3 reports the Spearman correlation coefficients between CIELCH parameters, iron oxide minerals semi-quantitative data, elemental iron, and PM_{10}. As can be observed, iron (Fe) is significantly linearly correlated with PM_{10} (+0.96), confirming that mineral dust is one of the main components in the analyzed samples. A high positive correlation between the height of the peaks at 480 nm and 535 nm and the concentration of iron is observed (respectively, +0.84 and +0.86) confirming the similar behavior shown in Figure 6 and proving the reliability of the semi-quantitative data on iron mineral oxides obtained from diffuse reflectance measurements. Among the two semi-quantitative data of iron oxide minerals, h_535 nm appears as the most significantly related to filter colors (+0.85 with chroma and –0.83 with hue). This result is extremely interesting because, as previously described in subsection 3.2, this peak is specific to hematite while the other peak (h_480nm) is associated with several other iron oxides, and especially goethite. An increase in chroma and a decrease in hue leads to a higher degree in the redness of the PM filters (see subsection 3.1), which is exactly the characteristic color of hematite (Rossman, 1996). As such, the semi-quantitative data on iron oxide minerals (especially hematite) are strongly related to PM filter colors (especially the red color), and both parameters are indicative of Saharan dust transport events.

3.4 Diagnosis and validation of Saharan mineral dust events

Figure 7 reports the dendrogram obtained from Ward's clustering analysis applied to the UV-Vis DRS results (CIELCH parameters and iron oxide minerals semi-quantitative data), and where two main clusters are identified. In particular, 15 PM samples belong to cluster 1, while the other 4 PM samples belong to cluster 2. These clusters are compared with PM_{10} data (normalized in air sampled volume, $\mu g/m^3$) in Figure 8 (a). Indeed, the association of mineral dust transport events has already been clearly related to significant increases in PM due to the considerable mass load of this component in particulate material owing to the large fraction of the coarse particles (Krasnov et al., 2014; Matassoni et al., 2011). In order to facilitate the Saharan Dust detection, the UV-Vis DRS results reported in the previous subsections are reported again in Figure 8(b) and Figure 8(c). The residence time spent by the air parcels over different areas before reaching the sampling site is also reported in Figure 9 for each PM sample.

Cluster 1 (highlighted in red) clearly identifies the Saharan dust events while cluster 2 (highlighted in green) identifies the non-Saharan dust events (Figure 8(a)). Indeed, the PM filters classified as cluster 1 are largely characterized by a higher value of PM_{10}, confirming a significant increase in PM mass load as a result of mineral dust contribution. This evidence is also supported by the color of the filters and semi-quantitative data of iron oxide minerals, (see Figures 8 (b,c)), whereas samples belonging to cluster 2 are more greyish owing to the lower concentration of iron mineral oxides, while samples belonging to cluster 1 are more brownish/reddish and with higher concentrations of iron mineral oxides. As a final not negligible data, these results agree with the outcome of the residence time analysis depicted in Figure 9 (a). The residence time analysis highlights how SN2, SN15, and SN19 samples belonging to cluster 2 are characterized by shorter residence times (less than 10%) over Africa than other PM filters (higher than 10%), suggesting uplift and rapid transport of mineral dust from the North-African desert without appreciable mixing with other aerosol sources.

Sample SN1 presents an exception being characterized by an elevated PM_{10} value and a residence time over Africa comparable to the samples belonging to the Saharan dust events cluster (cluster 1). Its assignment to the category of non-Saharan dust events, carried out only by UV-Vis DRS, is linked to its greyish color and to the low concentrations of iron oxide minerals. In order to justify this outcome, an in-depth analysis was carried out by satellite images retrieved from NASA's Earth Observing System Data and Information System (EOSDIS) (Behnke et al., 2019), shown in Figure 10. Whitish dust from the dried surface of Chott el-Jerid ephemeral lake (Figure 10(a)), was uplifted by the wind on 05/06/2016 (Figure 10(b)) and reached the receptor site on 08/06/2016 (from Figure 10(c) to Figure 10(f)), that is the first day of SN1 filter sampling period. Therefore, although the SN1 sample is significantly impacted by this Saharan dust transport event, its chemical-mineralogical composition is unusual compared to other PM samples due to the deficiency of iron oxide minerals, as evidenced by the grayish color of the examined filter.

After the classification of the Saharan dust events in the analyzed filters, some particular considerations can be drawn for some of the other samples, i.e. SN12 and SN19. SN12 is one of the PM filters more impacted by a Saharan dust events, as from its high PM_{10} concentration and its pronounced reddish color, as previously described in subsection 3.1. The latter observation may be explained by the higher value of residence time over Mauritania (> 4%), as reported in Figure 9 (b), whose area is known to be an important source of reddish hematite (Journet et al., 2014; Schlueter, 2006; Waele et al., 2019). As previously assessed, sample SN19 is clearly a PM sample not affected by Saharan dust transport. This filter presents the “whitest” color amongst the samples analysed, as shown by the highest luminescence value (L* = 73.23, look at Table 1) in the CIELAB/CIELCH colorimetric models. This result can be justified by a significantly long residence time over the Atlantic Ocean at low altitude (> 5%), as reported in Figure 9 (c), which presumably involves a strong influence of colorless sea salt component (mainly defined by sodium chloride and magnesium chloride) in the examined filter.

4. CONCLUSIONS

In this work, the feasibility of UV-Vis Diffuse Reflectance Spectroscopy for a rapid and non-destructive diagnosis of Saharan dust events in particulate matter filters has been described, assessed, and validated. This method has been applied to particulate matter filters sampled at high altitude (2550 m a.s.l.) in an area heavily impacted by Saharan mineral dust incursion events due to its proximity to North Africa (Sierra Nevada, Spain, 37.096 N, -3.387 W).

In particular, this analytical method allowed to identify unequivocally two absorption bands corresponding to a well-defined set of iron mineral oxides contained in Saharan dust: the absorption band at about 480 nm, representative of multiple iron oxide minerals (i.e., goethite, lepidocrocite, maghemite, ferrihydrite, feroxyhyte, akaganéite, and schwertmannite), and another at about 535 nm, specific for hematite. Through appropriate processing of the obtained reflectance spectra, it has been possible to obtain semi-quantitative data for these mineral oxides. Furthermore, starting from the reflectance measurements, it has been possible to quantitatively parameterize the filter coloring as a function of PM source.

The results obtained from this technique have been validated on the basis of the elemental iron concentration obtained by Proton Induced X-ray Emission (PIXE) analysis. Besides, it has been demonstrated the relation between the concentration of hematite increases and the higher reddish color of the filters with an increase in their PM_{10} content. Therefore, the UV-Vis DRS has been proven to be extremely useful for a fast, cheap, and unambiguous identification of Saharan mineral dust events in PM filters.

The results obtained have been finally proven on the basis of residence time analysis of back-trajectory ensembles, whose outcomes are in excellent agreement with those obtained by UV-Vis DRS, except for one PM sample with a peculiar chemical-mineralogical composition likely associated with the dried Chott el-Jerid Lake (Tunisia). Furthermore, some other samples have been explored

by associating the color and the semi-quantitative data of iron oxide minerals with their particular PM sources.

In conclusion, the UV-Vis DRS technique can be reliably adopted for Saharan dust events under certain conditions:

- The prevailing emission source of PM filters must be mineral dust. Indeed, a complex mixture of sources can alter the color and mineralogical composition of the sampled filters, making the identification of Saharan dust events extremely complicated; however, it is important to highlight that in this work weekly PM_{10} samples have been used, certainly affected by a complex mixture of emission sources and, despite this, reasonable outcomes have been achieved.
- Iron oxide minerals prove as efficient but also practically utilizable markers of Saharan mineral dust. This is valid in most cases even though, in this work, it has been highlighted that this spectroscopic technique is not capable to identify whitish sand events, characterized by low concentrations of iron oxide minerals.

ACKNOWLEDGEMENTS

This work has been carried out under the Spanish project FRESA (Impact of dust-laden African air masses and of stratospheric air masses in the Iberian Peninsula. Role of the Atlas Mountains, Ref: CGL2015-70741-R). Firstly, Lucas Alados-Arboledas (IISTA-CEAMA) is gratefully acknowledged for making possible the field campaign at the sampling site. A Heartfelt thanks to Sara Arcozzi, for her technical assistance on the Perkin Elmer Lambda 35 UV-Vis Spectrophotometer, and Christian Cingolani, Josep Mestres Sanna, and Adrià Simon Ortiz for the assistance in the experimental activity during their thesis work. Finally, the authors acknowledge the NOAA Air Resources Laboratory (ARL) for the provision of the HYSPLIT transport and dispersion model and/or READY website

(https://www.ready.noaa.gov) used in this publication and the European Centre for Medium-range Weather Forecast (ECMWF) for making available the ERA-Interim database.

REFERENCES

Akoglu, H. (2018). User's guide to correlation coefficients. Turkish Journal of Emergency Medicine, 18. https://doi.org/10.1016/j.tjem.2018.08.001

Alastuey, A., Querol, X., Aas, W., Lucarelli, F., Pérez, N., Moreno, T., … Yttri, K. E. (2016). Geochemistry of PM10 over Europe during the EMEP intensive measurement periods in summer 2012 and winter 2013. Atmos. Chem. Phys., 16(10), 6107–6129. https://doi.org/10.5194/acp-16-6107-2016

Alfaro, S., Lafon, S., Rajot, J., Formenti, P., Gaudichet, A., & Maillé, M. (2004). Iron oxides and light absorption by pure desert dust: An experimental study. Journal of Geophysical Research (Atmospheres), 109, 8208. https://doi.org/10.1029/2003JD004374

Arimoto, R., Balsam, W., & Schloesslin, C. (2002). Visible spectroscopy of aerosol particles collected on filters: Iron-oxide minerals. Atmospheric Environment, 36, 89–96. https://doi.org/10.1016/S1352-2310(01)00465-4

Ashbaugh, L. L., Malm, W. C., & Sadeh, W. Z. (1985). A residence time probability analysis of sulfur concentrations at grand Canyon National Park. Atmospheric Environment (1967), 19(8), 1263–1270. https://doi.org/https://doi.org/10.1016/0004-6981(85)90256-2

Barnaba, F., Bolignano, A., di Liberto, L., Morelli, M., Lucarelli, F., Nava, S., … Gobbi, G. P. (2017). Desert dust contribution to PM10 loads in Italy: Methods and recommendations addressing the relevant European Commission Guidelines in support to the Air Quality Directive 2008/50. Atmospheric Environment, 161. https://doi.org/10.1016/j.atmosenv.2017.04.038

528 Barrón, V., & Torrent, J. (1986). Use of the Kubelka—Munk theory to study the influence of iron
529 oxides on soil colour. Journal of Soil Science, 37(4), 499–510.

530 Behnke, J., Mitchell, A., & Ramapriyan, H. (2019). NASA's Earth Observing Data and Information
531 System – Near-Term Challenges. Data Science Journal, 18. https://doi.org/10.5334/dsj-2019-040

532 Blitz, J. P. (1998). Diffuse reflectance spectroscopy. Modern Techniques in Applied Molecular
533 Spectroscopy, 14, 185.

534 Bonasoni, P., Cristofanelli, P., Sandro, F., Gobbi, G. P., van Dingenen, R., Tositti, L., & Balkanski,
535 Y. (2003). Ozone and aerosol correlation during Saharan dust transport episodes at Mt. Cimone.

536 Brattich, E, Hernández-Ceballos, M. A., Cinelli, G., & Tositti, L. (2015a). Analysis of 210Pb peak
537 values at Mt. Cimone (1998–2011). Atmospheric Environment, 112, 136–147.
538 https://doi.org/https://doi.org/10.1016/j.atmosenv.2015.04.020

539 Brattich, Erika, Riccio, A., Tositti, L., Cristofanelli, P., & Bonasoni, P. (2015b). An outstanding
540 Saharan dust event at Mt. Cimone (2165 m asl, Italy) in March 2004. Atmospheric Environment, 113,
541 223–235.

542 Bristow, C. S., Hudson-Edwards, K. A., & Chappell, A. (2010). Fertilizing the Amazon and equatorial
543 Atlantic with West African dust. Geophysical Research Letters, 37(14).

544 Cabello, M., G. Orza, J., Dueñas, C., Liger, E., Gordo, E., & Cañete, S. (2016). Back-trajectory
545 analysis of African dust outbreaks at a coastal city in southern Spain: Selection of starting heights
546 and assessment of African and concurrent Mediterranean contributions. Atmospheric Environment,
547 140. https://doi.org/10.1016/j.atmosenv.2016.05.047

548 Calzolai, G., Chiari, M., García Orellana, I., Lucarelli, F., Migliori, A., Nava, S., & Taccetti, F.
549 (2006). The new external beam facility for environmental studies at the Tandetron accelerator of

LABEC. Nuclear Instruments and Methods in Physics Research Section B: Beam Interactions with Materials and Atoms, 249(1), 928–931. https://doi.org/https://doi.org/10.1016/j.nimb.2006.03.193

Caquineau, S., Gaudichet, A., Gomes, L., & Legrand, M. (2002). Mineralogy of Saharan dust transported over northwestern tropical Atlantic Ocean in relation to source regions. Journal of Geophysical Research: Atmospheres, 107(D15), AAC 4-1-AAC 4-12. https://doi.org/10.1029/2000JD000247

Chiari, M., Yubero, E., Calzolai, G., Lucarelli, F., Crespo, J., Galindo, N., … Nava, S. (2018). Comparison of PIXE and XRF analysis of airborne particulate matter samples collected on Teflon and quartz fibre filters. Nuclear Instruments and Methods in Physics Research Section B: Beam Interactions with Materials and Atoms, 417, 128–132. https://doi.org/https://doi.org/10.1016/j.nimb.2017.07.031

Chin, M., Diehl, T., Dubovik, O., Eck, T., Holben, B., Sinyuk, A., & Streets, D. (2009). Light absorption by pollution, dust, and biomass burning aerosols: A global model study and evaluation with AERONET measurements. Annales Geophysicae, 27. https://doi.org/10.5194/angeo-27-3439-2009

Cuevas, E., Gómez-Peláez, A. J., Rodríguez, S., Terradellas, E., Basart, S., García, R. D., … Alonso-Pérez, S. (2017). The pulsating nature of large-scale Saharan dust transport as a result of interplays between mid-latitude Rossby waves and the North African Dipole Intensity. Atmospheric Environment, 167, 586–602.

Cusack, M., Alastuey, A., Pérez, N., Pey, J., & Querol, X. (2012). Trends of particulate matter (PM2. 5) and chemical composition at a regional background site in the Western Mediterranean over the last nine years (2002–2010). Atmos. Chem. Phys, 12(18), 8341–8357.

572 Dee, D., P, de, Uppala, Simmons, Berrisford, Poli, P., … Vitart, F. (2011). The ERA-Interim
573 reanalysis: Configuration and performance of the data assimilation system. Quarterly Journal of the
574 Royal Meteorological Society, 137, 553–597. https://doi.org/10.1002/qj.828

575 Diapouli, E., Manousakas, M. I., Vratolis, S., Vasilatou, V., Pateraki, S., Bairachtari, K. A., …
576 Eleftheriadis, K. (2017). AIRUSE-LIFE +: estimation of natural source contributions to urban
577 ambient air PM10 and PM2. 5 concentrations in southern Europe – implications to compliance with
578 limit values. Atmos. Chem. Phys., 17(5), 3673–3685. https://doi.org/10.5194/acp-17-3673-2017

579 Dickerson, R., Kondragunta, S., Stenchikov, G., Civerolo, K., Doddridge, B., & Holben, B. (1997).
580 The impact of aerosol on solar UV radiation and photochemical smog. Science (New York, N.Y.),
581 278, 827–830. https://doi.org/10.1126/science.278.5339.827

582 Draxler, R. R. (2003). Evaluation of an Ensemble Dispersion Calculation. Journal of Applied
583 Meteorology, 42(2), 308–317. https://doi.org/10.1175/1520-
584 0450(2003)042<0308:EOAEDC>2.0.CO;2

585 EC Commission (2011). Staff Working Paper establishing guidelines for determination of
586 contributions from the re-suspension of particulates following winter sanding or salting of roads under
587 the Directive 2008/50/EC on ambient air quality and cleaner air for Europe. European Commission,
588 SEC. 2011; 2011:207.
589 http://ec.europa.eu/environment/air/quality/legislation/pdf/sec_2011_0207.pdf

590 EEA, Technical report No 10/2012 (2012). Particulate matter from natural sources and related
591 reporting under the EU Air Quality Directive in 2008 and 2009. ISBN: 978-92-9213-325-2.
592 https://www.eea.europa.eu/publications/particulate-matter-from-natural-sources

593 Escudero, M., Castillo, S., Querol, X., Avila, A., Alarcón, M., Viana, M. M., … Rodríguez, S. (2005).
594 Wet and dry African dust episodes over eastern Spain. Journal of Geophysical Research:
595 Atmospheres, 110(D18). https://doi.org/10.1029/2004JD004731

596 Escudero, M., Querol, X., Pey, J., Alastuey, A., Pérez, N., Ferreira, F., … Cuevas, E. (2007). A
597 methodology for the quantification of the net African dust load in air quality monitoring networks.
598 Atmospheric Environment, 41(26), 5516–5524.
599 https://doi.org/https://doi.org/10.1016/j.atmosenv.2007.04.047

600 EU (2008). Directive 2008/50/EC of the European Parliament and of the Council of 21 May 2008 on
601 ambient air quality and cleaner air for Europe. Official Journal of the European Union.

602 Fernandez, R. N., & Schulze, D. G. (1992). Munsell colors of soils simulated by mixtures of goethite
603 and hematite with kaolinite. Zeitschrift Für Pflanzenernährung Und Bodenkunde, 155(5), 473–478.

604 Flentje, H., Briel, B., Beck, C., Collaud Coen, M., Fricke, M., Cyrys, J., … Thomas, W. (2015).
605 Identification and monitoring of Saharan dust: An inventory representative for south Germany since
606 1997. Atmospheric Environment, 109, 87–96.
607 https://doi.org/https://doi.org/10.1016/j.atmosenv.2015.02.023

608 Formenti, P., Caquineau, S., Chevaillier, S., Klaver, A., Desboeufs, K., Rajot, J., … Briois, V. (2014).
609 Dominance of goethite over hematite in iron oxides of mineral dust from Western Africa: quantitative
610 partitioning by X-ray Absorption Spectroscopy. Journal of Geophysical Research: Atmospheres, 119.
611 https://doi.org/10.1002/2014JD021668

612 Formenti, P., Nava, S., Prati, P., Chevaillier, S., Klaver, A., Lafon, S., … Chiari, M. (2010). Self-
613 attenuation artifacts and correction factors of light element measurements by X-ray analysis:
614 Implication for mineral dust composition studies. Journal of Geophysical Research, 115.
615 https://doi.org/10.1029/2009JD012701

Formenti, P., Rajot, J., Desboeufs, K., Caquineau, S., Chevallier, S., Nava, S., … Highwood, E. (2008). Regional variability of the composition of mineral dust from western Africa: Results from the AMMA SOP0/DABEX and DODO field campaigns. J. Geophys. Res., 113. https://doi.org/10.1029/2008JD009903

Garrison, V. H., Shinn, E. A., Foreman, W. T., Griffin, D. W., Holmes, C. W., Kellogg, C. A., … Smith, G. W. (2003). African and Asian Dust: From Desert Soils to Coral Reefs. BioScience, 53(5), 469–480. https://doi.org/10.1641/0006-3568(2003)053[0469:AAADFD]2.0.CO;2

Ginoux, P. (2017). Warming or cooling dust? Nature Geoscience, 10(4), 246–248. https://doi.org/10.1038/ngeo2923

Gonçalves, Í. G., Petter, C. O., & Machado, J. L. (2012). Quantification of hematite and goethite concentrations in kaolin using diffuse reflectance spectroscopy: a new approach to Kubelka-Munk theory. Clays and Clay Minerals, 60(5), 473–483.

Goudie, A., & Middleton, N. (2006). Desert Dust in the Global System. Desert Dust in the Global System, 1–287. https://doi.org/10.1007/3-540-32355-4

Ibraheem, N., Hasan, M., Khan, R. Z., & Mishra, P. (2012). Understanding Color Models: A Review. ARPN Journal of Science and Technology, 2.

IDSO, S. (1981). Climatic change: The role of atmospheric dust. Special Paper of the Geological Society of America, 186, 207–215. https://doi.org/10.1130/SPE186-p207

ISO-CIE 11664-1-2019. Colorimetry - CIE standard colorimetric observers. Standard, International Organization for Standardization, Geneva, CH.

ISO-CIE 11664-2-2020. Colorimetry - Part 2: CIE standard illuminants. Standard, International Organization for Standardization, Geneva, CH.

638 ISO-CIE 11664-4-2019. Colorimetry - Part 4: CIE 1976 L*a*b* colour space. Standard, International
639 Organization for Standardization, Geneva, CH.

640 Israelevich, P., Ganor, E., Alpert, P., Kishcha, P., & Stupp, A. (2012). Predominant transport paths
641 of Saharan dust over the Mediterranean Sea to Europe. Journal of Geophysical Research:
642 Atmospheres, 117(D2).

643 Journet, E., Balkanski, Y., & Harrison, S. (2014). A new data set of soil mineralogy for dust-cycle
644 modeling. ATMOSPHERIC CHEMISTRY AND PHYSICS, 14, 3801–3816.
645 https://doi.org/10.5194/acp-14-3801-2014

646 Karanasiou, A., Moreno, N., Moreno, T., Viana, M., de Leeuw, F., & Querol, X. (2012). Health
647 effects from Sahara dust episodes in Europe: Literature review and research gaps. Environment
648 International, 47, 107–114. https://doi.org/10.1016/j.envint.2012.06.012

649 Krasnov, H., Katra, I., Koutrakis, P., & Friger, M. (2014). Contribution of dust storms to PM10 levels
650 in an urban arid environment. Journal of the Air & Waste Management Association (1995), 64, 89–
651 94. https://doi.org/10.1080/10962247.2013.841599

652 Kremers, J., Baraas, R., & Marshall, N. (2016). Human Color Vision. https://doi.org/10.1007/978-3-
653 319-44978-4

654 Lafon, S., Sokolik, I., Rajot, J., Caquineau, S., & Gaudichet, A. (2006). Characterization of iron
655 oxides in mineral dust aerosols: Implications for light absorption. Journal of Geophysical Research,
656 111. https://doi.org/10.1029/2005JD007016

657 Lin, J. (2012). Lagrangian Modeling of the Atmosphre: An Introduction. In Geophysical Monograph
658 Series (Vol. 200). https://doi.org/10.1029/2012GM001376

659 Linke, C., Möhler, O., Veres, A., Mohácsi, Á., Bozóki, Z., Szabó, G., & Schnaiter, M. (2006). Optical
660 properties and mineralogical composition of different Saharan mineral dust samples: a laboratory
661 study. Atmos. Chem. Phys., 6(11), 3315–3323. https://doi.org/10.5194/acp-6-3315-2006

662 Littmann, T., & Steinrücke, J. (1989). Atmospheric boundary conditions of recent Saharan dust influx
663 into Central Europe. GeoJournal, 18, 399–406. https://doi.org/10.1007/BF00772694

664 Lucarelli, F., Calzolai, G., Chiari, M., Giannoni, M., Mochi, D., Nava, S., & Carraresi, L. (2014). The
665 upgraded external-beam PIXE/PIGE set-up at LABEC for very fast measurements on aerosol
666 samples. Nuclear Instruments and Methods in Physics Research Section B: Beam Interactions with
667 Materials and Atoms, 318, 55–59. https://doi.org/https://doi.org/10.1016/j.nimb.2013.05.099

668 Lucarelli, F., Calzolai, G., Chiari, M., Nava, S., & Carraresi, L. (2018). Study of atmospheric aerosols
669 by IBA techniques: The LABEC experience. Nuclear Instruments and Methods in Physics Research
670 Section B: Beam Interactions with Materials and Atoms, 417, 121–127.
671 https://doi.org/https://doi.org/10.1016/j.nimb.2017.07.034

672 Lucarelli, F., Nava, S., Calzolai, G., Chiari, M., Udisti, R., & Marino, F. (2011). Is PIXE still a useful
673 technique for the analysis of atmospheric aerosols? The LABEC experience. X-Ray Spectrometry,
674 40, 162–167. https://doi.org/10.1002/xrs.1312

675 Lupu, A., & Maenhaut, W. (2002). Application and comparison of two statistical trajectory
676 techniques for identification of source regions of atmospheric aerosol species. Atmospheric
677 Environment, 36(36), 5607–5618. https://doi.org/https://doi.org/10.1016/S1352-2310(02)00697-0

678 Marconi, M., Sferlazzo, D. M., Becagli, S., Bommarito, C., Calzolai, G., Chiari, M., … Udisti, R.
679 (2014). Saharan dust aerosol over the central Mediterranean Sea: PM10 chemical composition and
680 concentration versus optical columnar measurements. Atmos. Chem. Phys., 14(4), 2039–2054.
681 https://doi.org/10.5194/acp-14-2039-2014

682 Matassoni, L., Pratesi, G., Centioli, D., Cadoni, F., Lucarelli, F., Nava, S., & Malesani, P. (2011).
683 Saharan dust contribution to PM 10, PM 2.5 and PM 1 in urban and suburban areas of Rome: A
684 comparison between single-particle SEM-EDS analysis and whole-sample PIXE analysis. Journal of
685 Environmental Monitoring : JEM, 13, 732–742. https://doi.org/10.1039/c0em00535e

686 Menéndez, I., Díaz-Hernández, J. L., Mangas, J., Alonso, I., & Sánchez-Soto, P. J. (2007). Airborne
687 dust accumulation and soil development in the North-East sector of Gran Canaria (Canary Islands,
688 Spain). Journal of Arid Environments, 71(1), 57–81.
689 https://doi.org/https://doi.org/10.1016/j.jaridenv.2007.03.011

690 Middleton, N., & Goudie, A. (2002). Saharan dust: Sources and trajectories. Transactions of the
691 Institute of British Geographers, 26, 165–181. https://doi.org/10.1111/1475-5661.00013

692 Molinaroli, E., & Masiol, M. (2006). Particolato atmosferico e ambiente mediterraneo. Il caso delle
693 polveri sahariane.

694 Nava, S., Becagli, S., Calzolai, G., Chiari, M., Lucarelli, F., Prati, P., … Vecchi, R. (2012). Saharan
695 dust impact in central Italy: An overview on three years elemental data records. Atmospheric
696 Environment, 60, 444–452. https://doi.org/https://doi.org/10.1016/j.atmosenv.2012.06.064

697 WHO (2006). WHO Air quality guidelines for particulate matter, ozone, nitrogen dioxide and sulfur
698 dioxide : global update 2005 : summary of risk assessment (p. WHO/SDE/PHE/OEH/06.02). p.
699 WHO/SDE/PHE/OEH/06.02. World Health Organization.

700 Ojeda, C. B., & Rojas, F. S. (2013). Recent applications in derivative ultraviolet/visible absorption
701 spectrophotometry: 2009–2011: a review. Microchemical Journal, 106, 1–16.

702 Orza, J. A. G., Cabello, M., Galiano, V., Vermeulen, A. T., & Stein, A. F. (2013). The Association
703 Between the North Atlantic Oscillation and the Interannual Variability of the Tropospheric Transport

704 Pathways in Western Europe. In Lagrangian Modeling of the Atmosphere (pp. 127–142).
705 https://doi.org/10.1029/2012GM001315

706 Pandey, A., Shetty, N. J., & Chakrabarty, R. K. (2019). Aerosol light absorption from optical
707 measurements of PTFE membrane filter samples: sensitivity analysis of optical depth measures.
708 Atmos. Meas. Tech., 12(2), 1365–1373. https://doi.org/10.5194/amt-12-1365-2019

709 Petzold, A., & Schönlinner, M. (2004). Multi-angle absorption photometry—a new method for the
710 measurement of aerosol light absorption and atmospheric black carbon. Journal of Aerosol Science,
711 35(4), 421–441. https://doi.org/https://doi.org/10.1016/j.jaerosci.2003.09.005

712 Prospero, J., Schmitt, R., Cuevas, E., Savoie, D., Graustein, W., Turekian, K., … II, H. (1995).
713 Temporal variability of summer-time ozone and aerosols in the free troposphere over the eastern
714 North Atlantic. Geophysical Research Letters, 22, 2925–2928. https://doi.org/10.1029/95GL02791

715 Putaud, J.-P., van Dingenen, R., Dell'Acqua, A., Raes, F., Matta, E., Decesari, S., … Fuzzi, S. (2004).
716 Size-segregated aerosol mass closure and chemical composition in Monte Cimone (I) during
717 MINATROC.

718 Querol, X., Tobías, A., Pérez, N., Karanasiou, A., Amato, F., Stafoggia, M., … Alastuey, A. (2019).
719 Monitoring the impact of desert dust outbreaks for air quality for health studies. Environment
720 International, 130, 104867. https://doi.org/https://doi.org/10.1016/j.envint.2019.05.061

721 R Core Team (2019). R: A language and environment for statistical computing. R Foundation for
722 Statistical Computing, Vienna, Austria. URL https://www.R-project.org/.

723 Reicher, N., Budke, C., Eickhoff, L., Raveh-Rubin, S., Kaplan-Ashiri, I., Koop, T., & Rudich, Y.
724 (2019). Size-dependent ice nucleation by airborne particles during dust events in the eastern
725 Mediterranean. Atmos. Chem. Phys., 19(17), 11143–11158. https://doi.org/10.5194/acp-19-11143-
726 2019

727 Remoundaki, E., Bourliva, A., Kokkalis, P., Mamouri, R. E., Papayannis, A., Grigoratos, T., …
728 Tsezos, M. (2011). PM10 composition during an intense Saharan dust transport event over Athens
729 (Greece). Science of The Total Environment, 409(20), 4361–4372.
730 https://doi.org/https://doi.org/10.1016/j.scitotenv.2011.06.026

731 Riccio, A., Chianese, E., Tositti, L., Baldacci, D., & Sandrini, S. (2009). Modeling the transport of
732 Saharan dust toward the Mediterranean region: an important issue for its ecological implications.
733 Ecological Questions, 11, 65–72.

734 Rodríguez, S., Calzolai, G., Chiari, M., Nava, S., García, M. I., López-Solano, J., … Querol, X.
735 (2020). Rapid changes of dust geochemistry in the Saharan Air Layer linked to sources and
736 meteorology. Atmospheric Environment, 223, 117186.
737 https://doi.org/https://doi.org/10.1016/j.atmosenv.2019.117186

738 Rolph, G., Stein, A., & Stunder, B. (2017). Real-time Environmental Applications and Display
739 sYstem: READY. Environmental Modelling & Software, 95, 210–228.
740 https://doi.org/https://doi.org/10.1016/j.envsoft.2017.06.025

741 Rossman, G. (1996). Why hematite is red: Correlation of optical absorption intensities and magnetic
742 moments of Fe3+ minerals. 5, 23–27.

743 Schafer, R. (2011). What Is a Savitzky-Golay Filter? [Lecture Notes]. IEEE Signal Processing
744 Magazine - IEEE SIGNAL PROCESS MAG, 28, 111–117.
745 https://doi.org/10.1109/MSP.2011.941097

746 Scheinost, A., Chavernas, A., Barrón, V., & Torrent, J. (1998). Use and limitations of second-
747 derivative diffuse reflectance spectroscopy in the visible to near-infrared range to identify and
748 quantify Fe oxides in soils. Clays and Clay Minerals, 46, 528–536.
749 https://doi.org/10.1346/CCMN.1998.0460506

Schloss, K. B., Lessard, L., Racey, C., & Hurlbert, A. C. (2018). Modeling color preference using color space metrics. Vision Research, 151, 99–116. https://doi.org/https://doi.org/10.1016/j.visres.2017.07.001

Schlueter, T. (2006). Geological Atlas of Africa: With Notes on Stratigraphy, Tectonics, Economic Geology, Geohazards and Geosites of Each Country. https://doi.org/10.1007/3-540-29145-8

Sellitto, V., Barrón, V., Palumbo, G., Salzano, R., & Colombo, C. (2008). Uso della spettrometria di riflettanza diffusa (DRS) e bi-direzionale (BRF) per lo studio dei suoli vulcanici europei.

Sellitto, V. M., Fernandes, R. B. A., Barrón, V., & Colombo, C. (2009). Comparing two different spectroscopic techniques for the characterization of soil iron oxides: Diffuse versus bi-directional reflectance. Geoderma, 149(1–2), 2–9.

Shao, L., Li, W., Yang, S., Shi, Z., & Lü, S. (2007). Mineralogical characteristics of airborne particles collected in Beijing during a severe Asian dust storm period in spring 2002. Science in China Series D: Earth Sciences, 50(6), 953–959. https://doi.org/10.1007/s11430-007-0035-7

Shen, Z. X., Cao, J. J., Zhang, X. Y., Arimoto, R., Ji, J. F., Balsam, W. L., … Li, X. X. (2006). Spectroscopic analysis of iron-oxide minerals in aerosol particles from northern China. Science of the Total Environment, 367(2–3), 899–907.

Sherman, D. M., & Waite, T. D. (1985). Electronic spectra of Fe3+ oxides and oxide hydroxides in the near IR to near UV. American Mineralogist, 70(11–12), 1262–1269. Retrieved from http://pubs.er.usgs.gov/publication/70012311

Shi, Z., Krom, M. D., Jickells, T. D., Bonneville, S., Carslaw, K. S., Mihalopoulos, N., … Benning, L. G. (2012). Impacts on iron solubility in the mineral dust by processes in the source region and the atmosphere: A review. Aeolian Research, 5, 21–42. https://doi.org/https://doi.org/10.1016/j.aeolia.2012.03.001

773 Shinn, E. A., Smith, G. W., Prospero, J. M., Betzer, P., Hayes, M. L., Garrison, V., & Barber, R. T.
774 (2000). African dust and the demise of Caribbean Coral Reefs. Geophysical Research Letters, 27(19),
775 3029–3032. https://doi.org/10.1029/2000GL011599

776 Sokolik, I. N., & Toon, O. B. (1999). Incorporation of mineralogical composition into models of the
777 radiative properties of mineral aerosol from UV to IR wavelengths. Journal of Geophysical Research:
778 Atmospheres, 104(D8), 9423–9444. https://doi.org/10.1029/1998JD200048

779 Soleimani, Z., Teymouri, P., Darvishi Boloorani, A., Mesdaghinia, A., Middleton, N., & Griffin, D.
780 W. (2020). An overview of bioaerosol load and health impacts associated with dust storms: A focus
781 on the Middle East. Atmospheric Environment, 223, 117187.
782 https://doi.org/https://doi.org/10.1016/j.atmosenv.2019.117187

783 Stafoggia, M., Zauli-Sajani, S., Pey, J., Samoli, E., Alessandrini, E., Basagaña, X., … Díaz, J. (2016).
784 Desert dust outbreaks in Southern Europe: contribution to daily PM10 concentrations and short-term
785 associations with mortality and hospital admissions. Environmental Health Perspectives, 124(4),
786 413–419.

787 Stein, A. F., Draxler, R. R., Rolph, G. D., Stunder, B. J. B., Cohen, M. D., & Ngan, F. (2015).
788 NOAA's HYSPLIT Atmospheric Transport and Dispersion Modeling System. Bulletin of the
789 American Meteorological Society, 96(12), 2059–2077. https://doi.org/10.1175/BAMS-D-14-00110.1

790 Stohl, A. (1998). Computation, accuracy and applications of trajectories—A review and bibliography.
791 Atmospheric Environment, 32(6), 947–966. https://doi.org/https://doi.org/10.1016/S1352-
792 2310(97)00457-3

793 Szalai, Z., Kiss, K., Jakab, G., Sipos, P., Belucz, B., & Németh, T. (2013). The use of UV-VIS-NIR
794 reflectance spectroscopy to identify iron minerals. Astronomische Nachrichten, 334(9), 940–943.

795 Torrent, J., & Barrón, V. (2002). Diffuse Reflectance Spectroscopy of Iron Oxides. Encyclopedia of
796 Surface and Colloid Science, 1.

797 Torrent, J., & Barrón, V. (2008). Methods of Soil Analysis. Part 5. Mineralogical Methods, Chapter
798 13 Diffuse Reflectance Spectroscopy, SSSA Book Series, No. 5. USA, 367–385.

799 Tositti, L., Brattich, E., Cinelli, G., & Baldacci, D. (2014). 12 years of 7Be and 210Pb in Mt. Cimone,
800 and their correlation with meteorological parameters. Atmospheric Environment, 87, 108–122.
801 https://doi.org/https://doi.org/10.1016/j.atmosenv.2014.01.014

802 Usher, C. R., Michel, A. E., & Grassian, V. H. (2003). Reactions on mineral dust. Chemical Reviews,
803 103(12), 4883–4940.

804 van den Berg, R., Hoefsloot, H., Westerhuis, J., Smilde, A., & van der Werf, M. (2006). Van den
805 Berg RA, Hoefsloot HCJ, Westerhuis JA, Smilde AK, Van der Werf MJ.. Centering, scaling, and
806 transformations: improving the biological information content of metabolomics data. BMC Genomics
807 7: 142-157. BMC Genomics, 7, 142. https://doi.org/10.1186/1471-2164-7-142

808 Waele, B. de, Aitken, A., Mourik, M. van, Laab Laab, K. O., Elhacen Ould Med Yeslem, M., &
809 Mohamedou, T. (2019). From a Mining Mindset to Regional Discovery: A Case Study for Hematite
810 Iron Ore Exploration in Mauritania. ASEG Extended Abstracts, 2019(1), 1–3.
811 https://doi.org/10.1080/22020586.2019.12073145

812 Ward, J. H. (1963). Hierarchical groupings to optimize an objective function. J. Am. Stat. Assoc.,
813 234–244.

814 Xu, J., DuBois, D., Pitchford, M., Green, M., & Etyemezian, V. (2006). Attribution of sulfate aerosols
815 in Federal Class I areas of the western United States based on trajectory regression analysis.
816 Atmospheric Environment, 40(19), 3433–3447.
817 https://doi.org/https://doi.org/10.1016/j.atmosenv.2006.02.009

FIGURES:

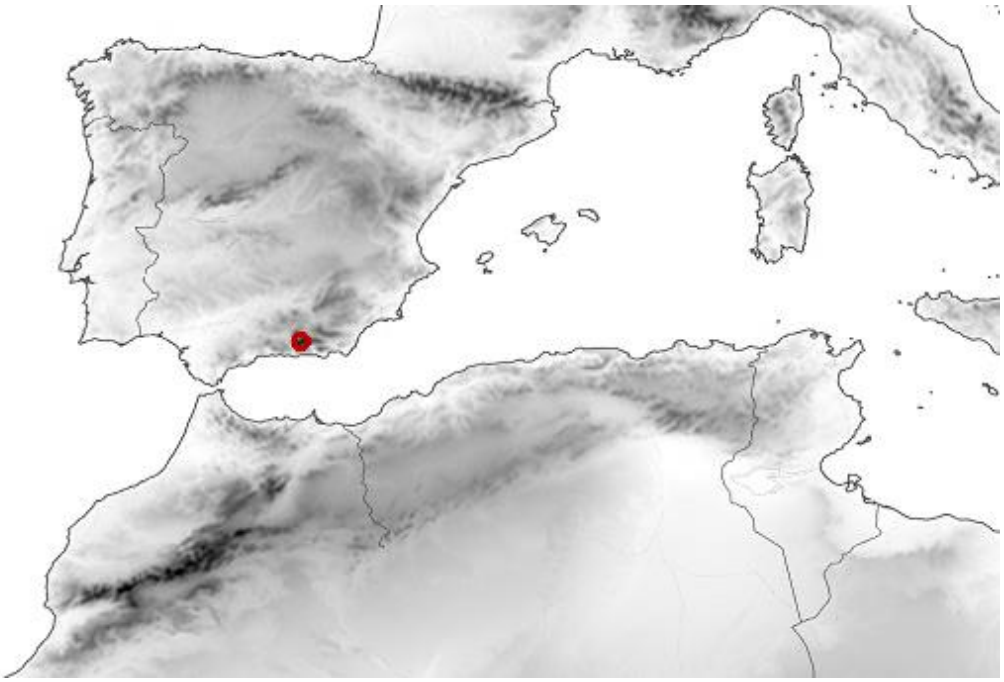

Figure 1. Map and location of Sierra Nevada sampling station.

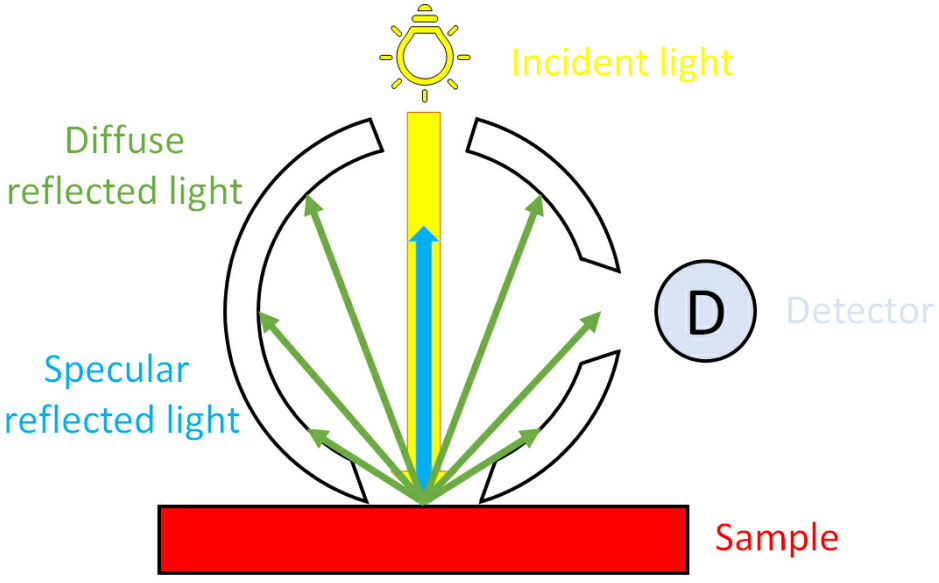

Figure 2. Scheme of the integrating sphere, 0°/d geometry. The UV-Vis incident light hits the sample perpendicularly. Any specular component of reflection from the sample is excluded from measurement since this component is directed out of the sphere through the transmittance sample entrance port and, therefore, the detector only measures the diffuse reflectance component.

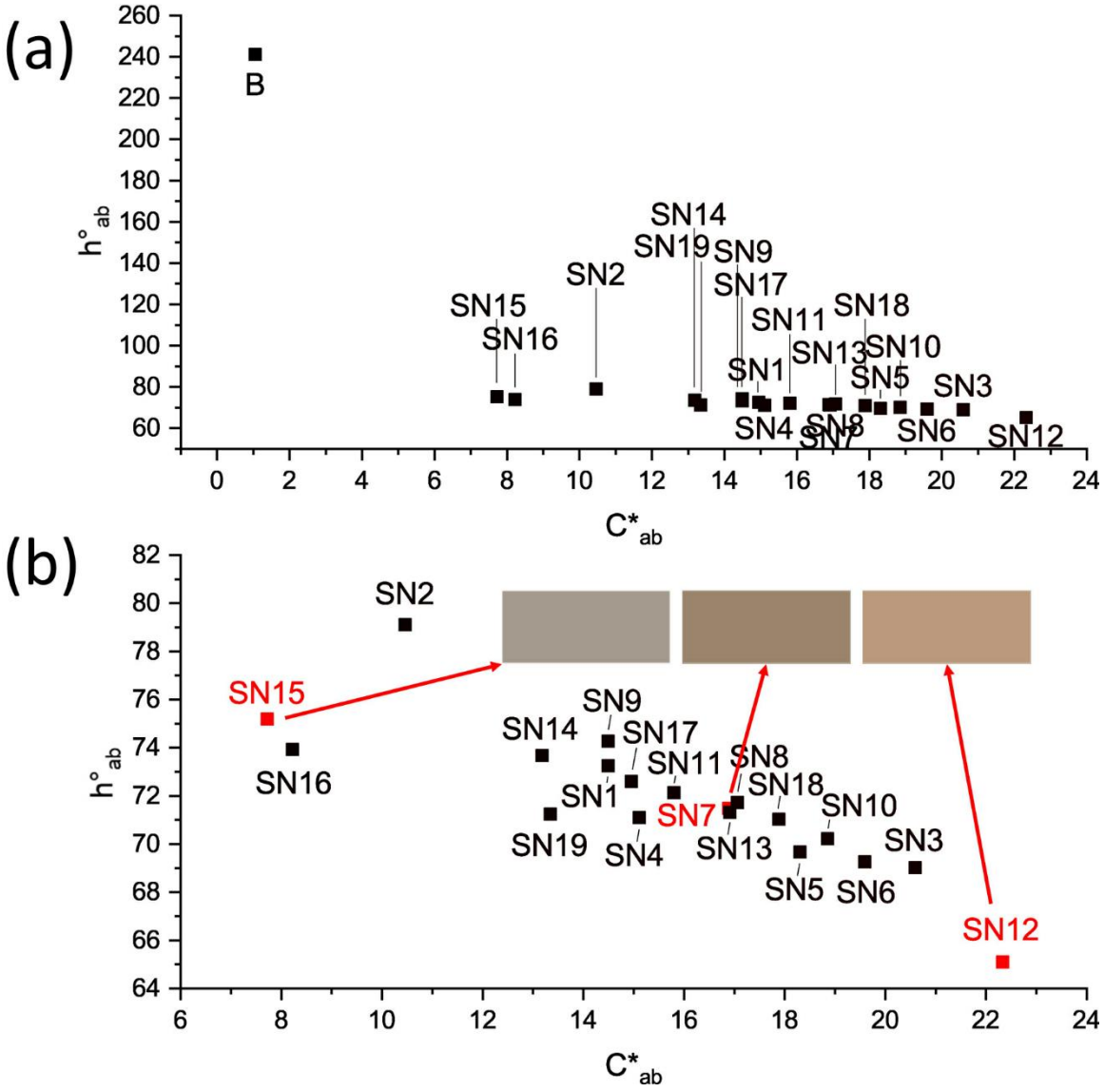

826

827 Figure 3. (a) Graphic representation of blank filter (B) and sampled filters (SN1, …SN19) based on
828 chroma (C_{ab}^*) and hue (h_{ab}°). (b) Zoomed plot on sampled filters. The colors of three specific samples
829 (SN15, SN7, SN12) are shown.

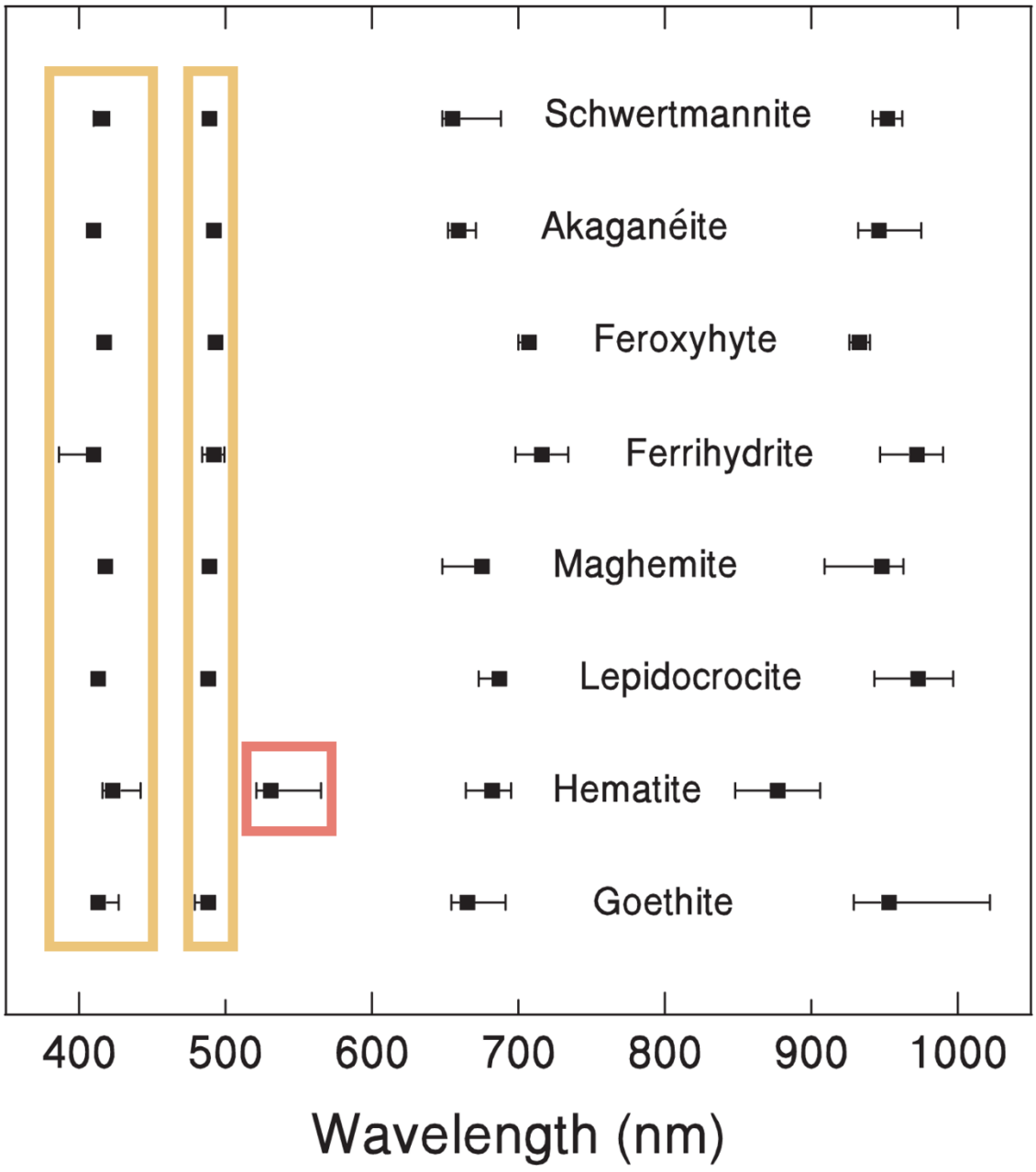

Figure 4. Median and range of the UV-Vis absorption bands of some iron oxide minerals in the second derivative of K-M function spectra, adapted from Torrent & Barrón, 2008. It can be seen that below 600 nm, there are three absorpion bands at around 420, 480, and 535 nm.

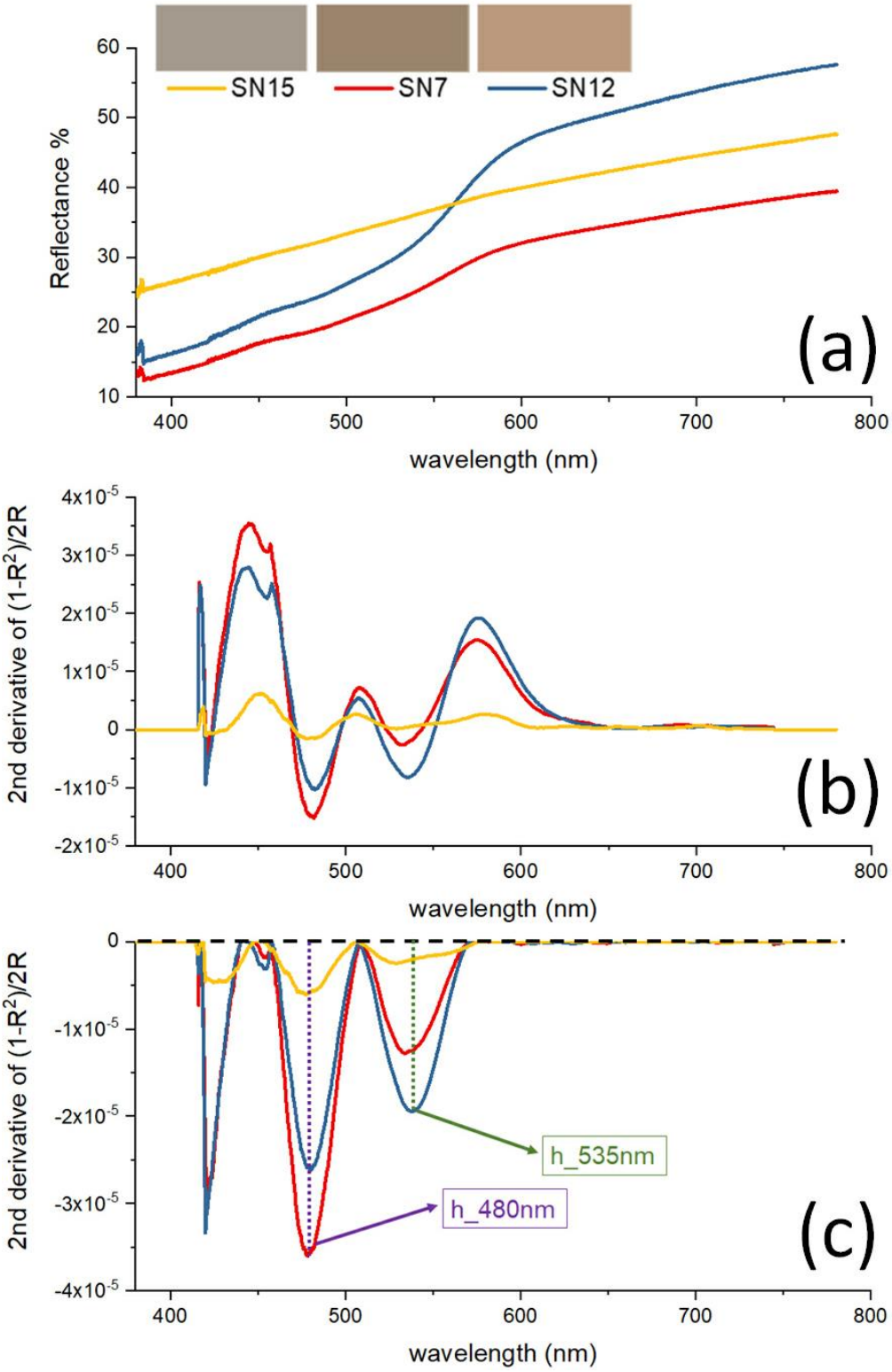

834

835 Figure 5. Reflectance spectra (a), Savitzky-Golay second derivative of Kubelka-Munk (K-M)
836 function spectra (b), and baseline subtraction and quantification of relevant peak heights (c) for SN15
837 (grayish filter), SN7 (brownish filter), and SN12 (reddish filter).

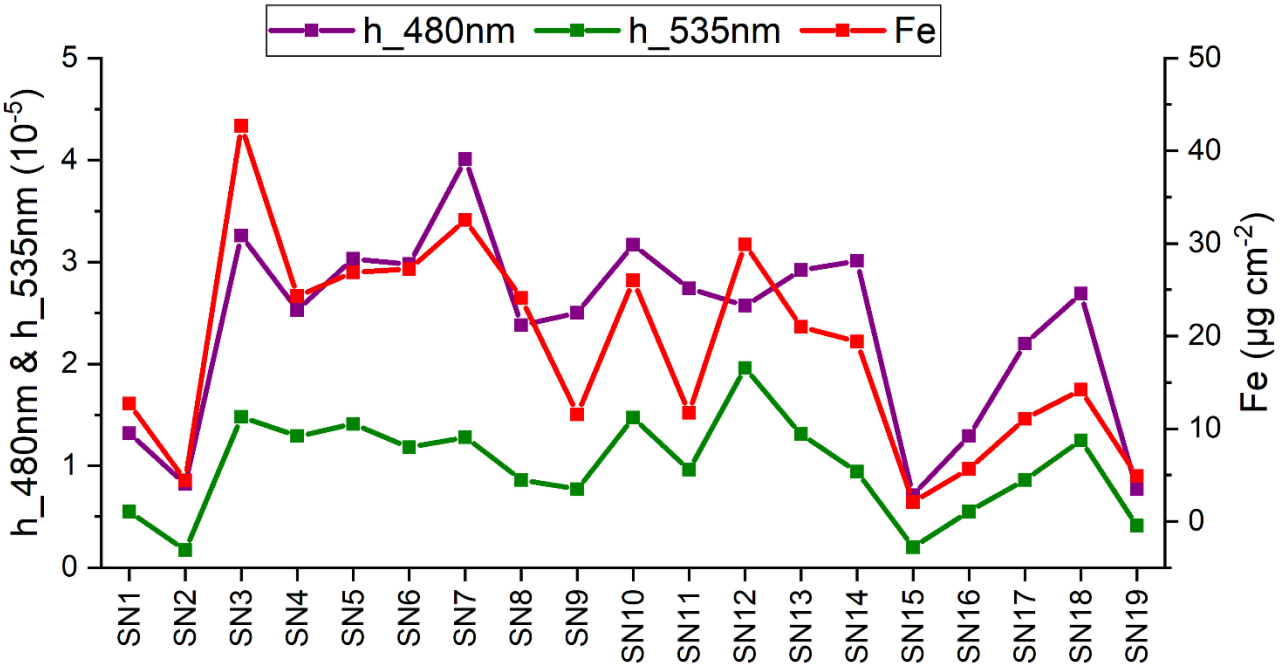

Figure 6. Sample series of h_480nm (semi-quantitative data of several iron oxide minerals, mainly goethite), h_535nm (semi-quantitative data of hematite), and elemental iron concentration (Fe).

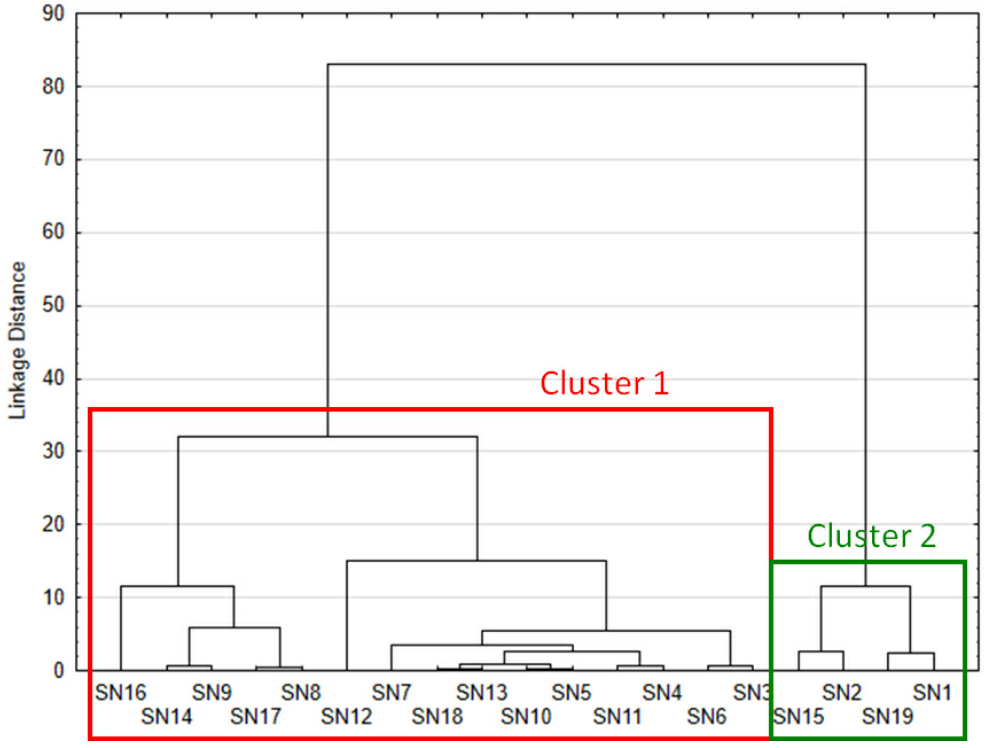

Figure 7. Dendrogram of Ward's hierarchical clustering method starting from CIELCH parameters and semi-quantitative data of iron oxide minerals. The clustering solution with two clusters is highlighted by squares.

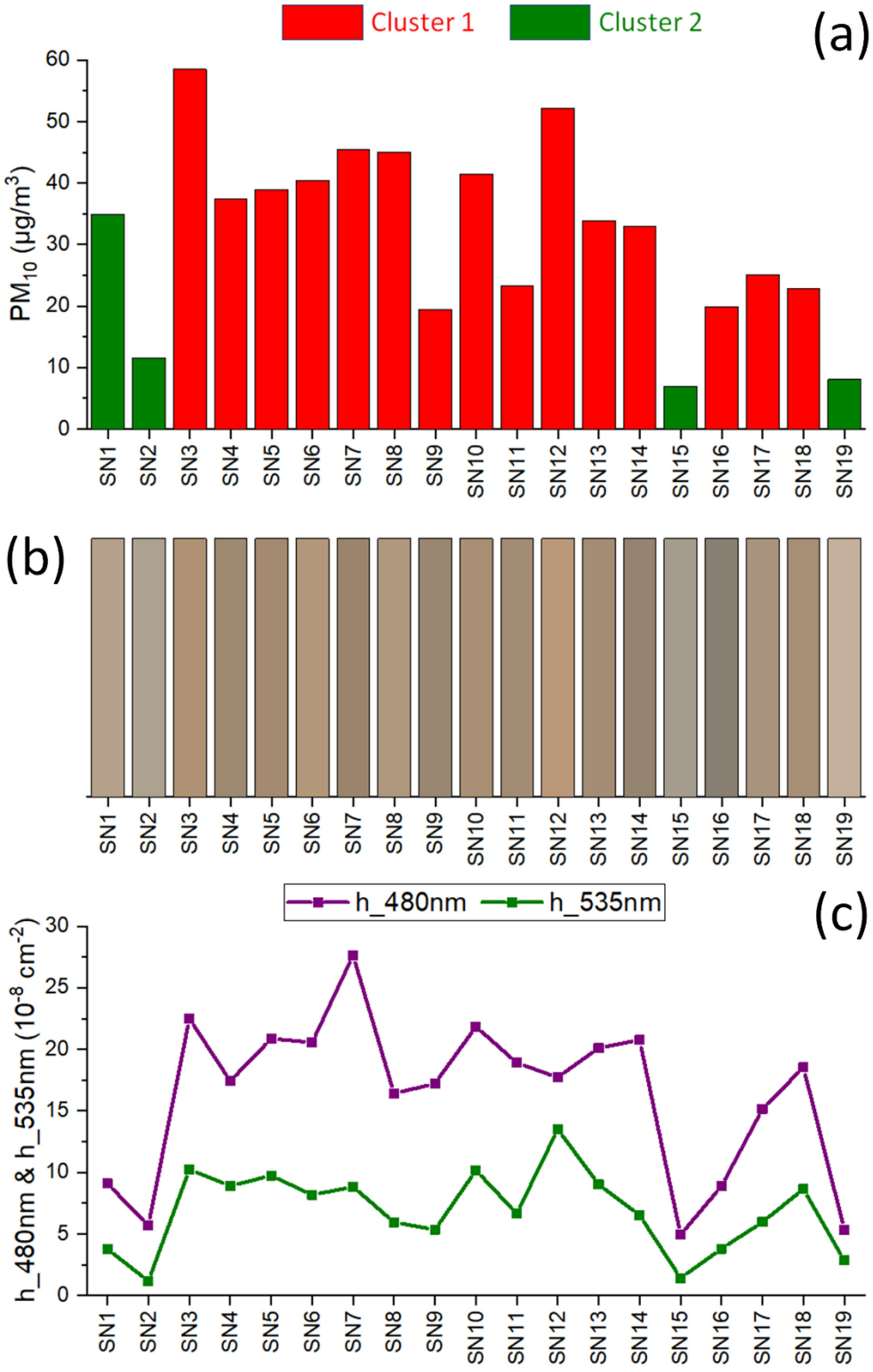

Figure 8. (a) Sample series of PM_{10} data ($\mu g/m^3$) with the association of PM filters to the respective clusters (cluster 1 and cluster 2). (b) Display of PM filters colors, look at subsection 3.1. (c) Sample series of h_480nm (semi-quantitative data of several iron oxide minerals) and h_535nm (hematite), look at subsection 3.2.

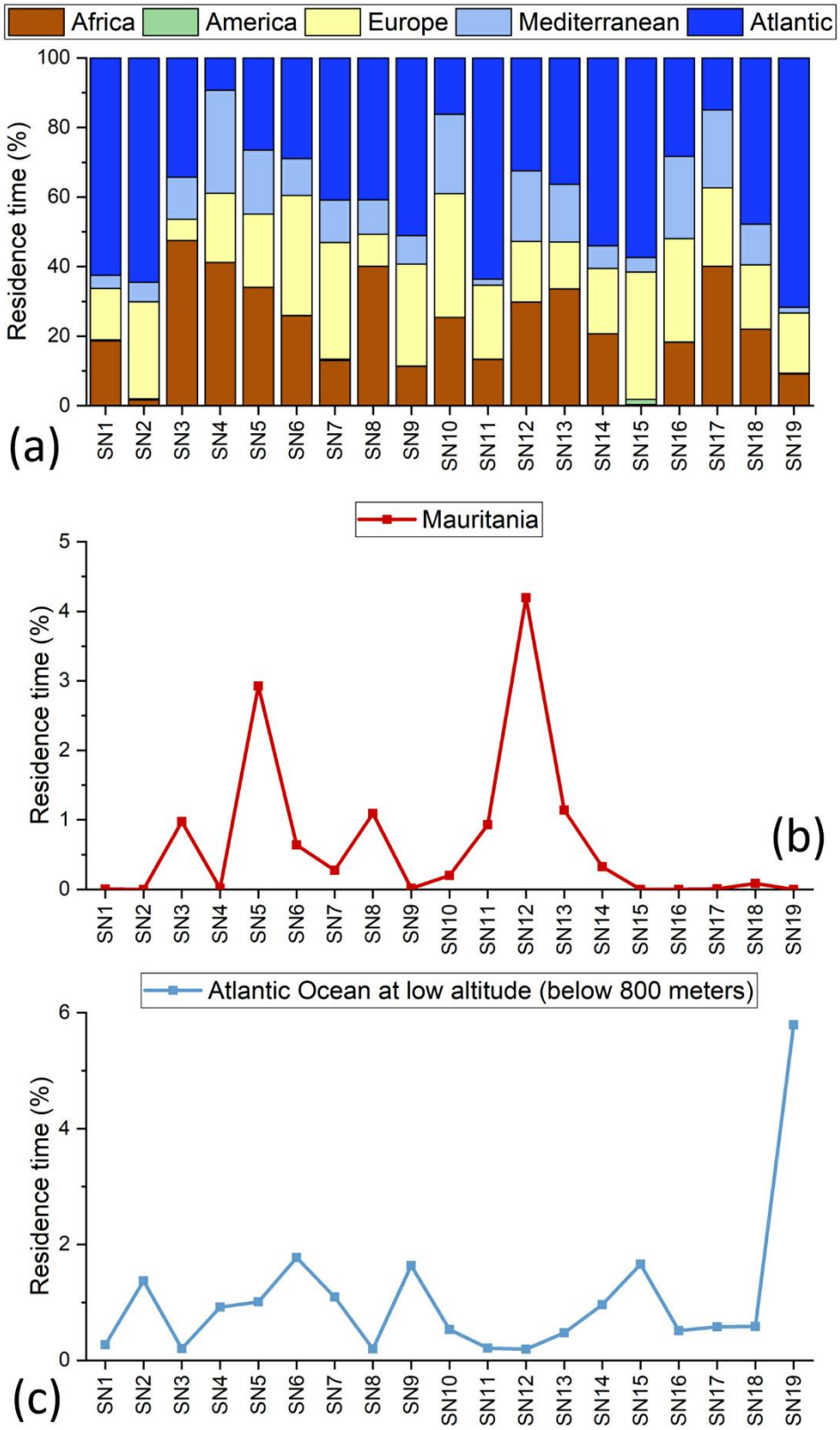

Figure 9. (a) Stacked bar chart of the percentage residence time over each examined region and PM filter; Sample series of residence time over Mauritania (b) and the Atlantic Ocean, below 800 meters (c).

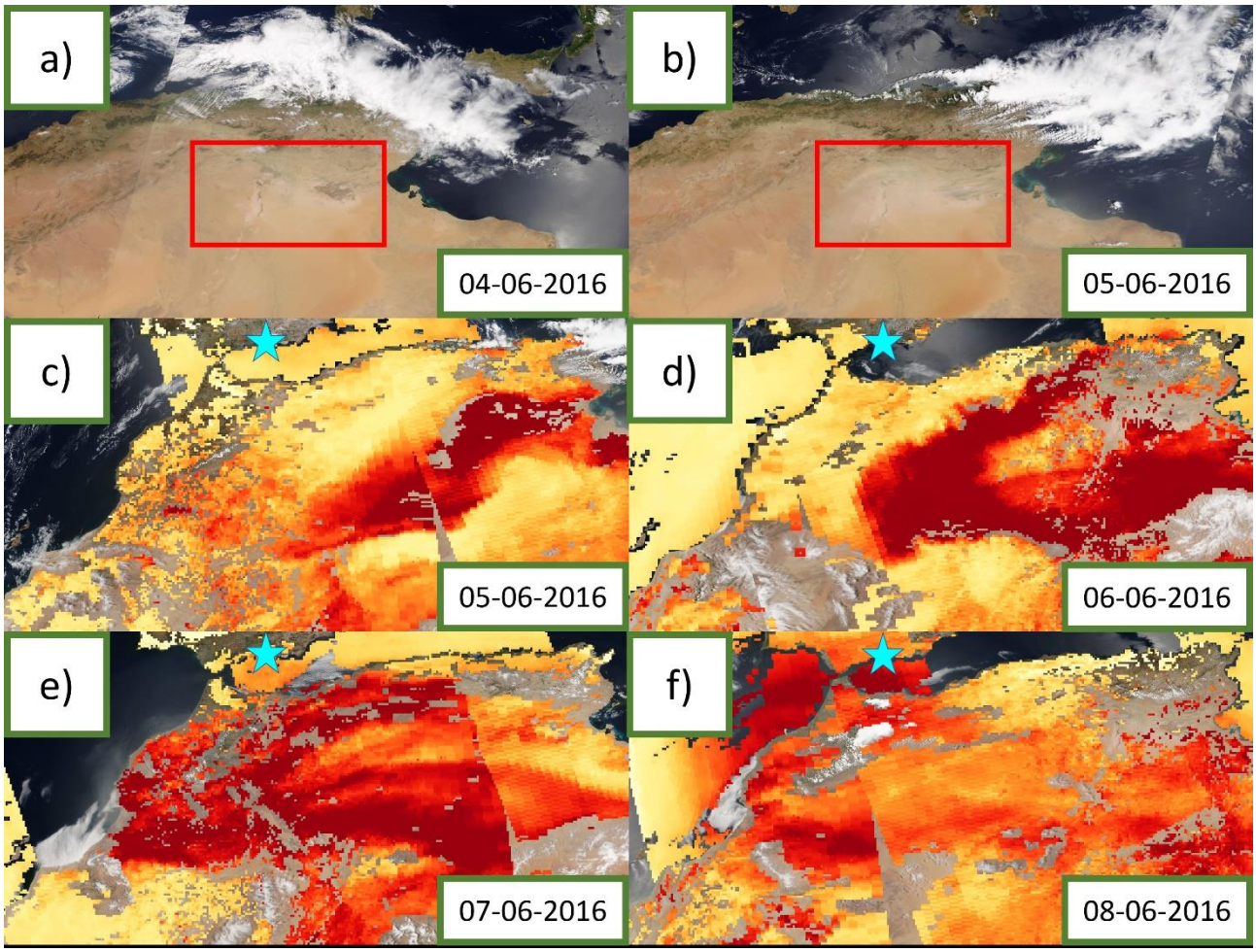

Figure 10. Corrected reflectance (True Color) Terra/MODIS snapshots for 4 June 2016 (a) and 5 June 2016 (b); Merged DT/DB Aerosol Optical Depth (Land and Ocean) Aqua/MODIS snapshots from 5 June 2016 (c) to 8 June 2016 (f). Higher AOD values are indicated by a more reddish color and allow following the dust plume transport. The red square in a) and b) highlights the Chott el-Jerid Lake (Tunisia) while the light blue star in c), d), e), and f) indicates the PM sampling station in Sierra Nevada (37.096 N, -3.387 W, 2550 m a.s.l.). Images have been retrieved from the NASA EOSDIS, worldview tool at https://worldview.earthdata.nasa.gov.

TABLES:

Table 1. Average values and standard deviations (numbers in brackets) of the colorimetric parameters for the analyzed samples. The colors obtained from the conversion to RGB color model by the online tool nix Color Sensor (https://www.nixsensor.com/free-color-converter/) are displayed in the last column of this table.

Sample	L*	a*	b*	C_{ab}*	h_{ab}°	Color
B	95.46 (0.11)	-0.51 (0.05)	-0.92 (0.13)	1.05 (0.14)	241.15 (0.81)	
SN1	67.49 (2.68)	4.14 (1.19)	13.89 (4.42)	14.49 (4.57)	73.26 (0.64)	
SN2	66.85 (3.60)	1.99 (0.43)	10.27 (1.08)	10.46 (1.13)	79.11 (1.53)	
SN3	62.63 (3.07)	7.37 (0.56)	19.23 (1.36)	20.59 (1.47)	69.03 (0.11)	
SN4	58.53 (2.46)	4.86 (1.55)	14.31 (4.99)	15.11 (5.22)	71.10 (0.71)	
SN5	59.27 (2.79)	6.33 (0.09)	17.16 (1.64)	18.30 (1.56)	69.67 (1.66)	
SN6	64.43 (2.91)	6.84 (0.46)	18.35 (3.35)	19.59 (3.28)	69.27 (2.52)	
SN7	56.77 (2.12)	5.36 (0.39)	16.02 (1.22)	16.89 (1.28)	71.48 (0.14)	
SN8	64.35 (1.41)	5.37 (1.63)	16.20 (4.63)	17.06 (4.90)	71.72 (0.38)	
SN9	57.51 (3.59)	3.94 (0.51)	13.94 (1.26)	14.49 (1.35)	74.27 (0.70)	
SN10	61.20 (3.26)	6.41 (1.31)	17.72 (2.97)	18.85 (3.23)	70.22 (0.79)	
SN11	59.83 (3.63)	4.86 (0.81)	15.04 (2.11)	15.80 (2.25)	72.13 (0.89)	
SN12	65.59 (0.76)	9.41 (1.52)	20.24 (2.92)	22.33 (3.28)	65.11 (0.65)	
SN13	60.28 (3.57)	5.43 (0.80)	16.02 (1.76)	16.91 (1.93)	71.31 (0.78)	
SN14	56.44 (1.09)	3.72 (0.95)	12.65 (2.98)	13.18 (3.13)	73.68 (0.49)	
SN15	64.91 (2.89)	1.94 (0.32)	7.47 (1.86)	7.72 (1.88)	75.19 (1.56)	
SN16	53.75 (2.55)	2.25 (0.27)	7.90 (1.52)	8.22 (1.53)	73.93 (1.58)	
SN17	62.68 (2.65)	4.46 (0.53)	14.27 (2.03)	14.95 (2.09)	72.60 (0.90)	
SN18	61.01 (2.99)	5.80 (0.09)	16.91 (1.04)	17.88 (1.00)	71.04 (0.98)	
SN19	73.23 (2.41)	4.20 (0.56)	12.63 (2.16)	13.34 (1.97)	71.24 (4.53)	

878 Table 2. Average values and standard deviations (numbers in brackets) of the semi-quantitative data
879 of mixed iron oxide minerals (h_480nm) and hematite (h_535 nm).

Sample	**h_480nm (10^{-5})**	**h_530nm (10^{-5})**
B	0.025 (0.009)	0.011 (0.005)
SN1	1.32 (0.37)	0.55 (0.08)
SN2	0.83 (0.16)	0.17 (0.04)
SN3	3.27 (0.71)	1.49 (0.20)
SN4	2.53 (1.20)	1.29 (0.17)
SN5	3.03 (0.03)	1.42 (0.06)
SN6	2.99 (0.27)	1.19 (0.19)
SN7	4.01 (0.38)	1.28 (0.11)
SN8	2.38 (0.90)	0.87 (0.08)
SN9	2.50 (0.05)	0.78 (0.16)
SN10	3.17 (0.11)	1.48 (0.09)
SN11	2.74 (0.10)	0.97 (0.18)
SN12	2.57 (0.10)	1.96 (0.22)
SN13	2.92 (0.62)	1.31 (0.33)
SN14	3.02 (0.64)	0.95 (0.15)
SN15	0.72 (0.46)	0.21 (0.13)
SN16	1.29 (0.15)	0.55 (0.26)
SN17	2.20 (0.06)	0.87 (0.19)
SN18	2.69 (0.52)	1.26 (0.31)
SN19	0.78 (0.18)	0.41 (0.09)

880
881
882
883
884
885
886
887
888

Table 3. Spearman correlation coefficients obtained for each pair of variables. L^* = CIELAB lightness, C_{ab}* = CIELAB chroma, h_{ab}° = CIELAB hue, Fe = elemental iron, PM_{10} = particulate matter, h _480nm = semi-quantitative data of mixed iron oxide minerals, h_535nm= semi-quantitative data of hematite.

	L*	C_{ab}*	h_{ab}°	Fe	PM_{10}	h_480nm	h_535nm
L*	1.00						
C_{ab}*	0.08	1.00					
h_{ab}°	-0.11	-0.90	1.00				
Fe	-0.20	0.85	-0.80	1.00			
PM_{10}	-0.11	0.81	-0.74	0.96	1.00		
h_480nm	-0.47	0.69	-0.60	0.84	0.75	1.00	
h_535nm	-0.28	0.85	-0.83	0.86	0.81	0.81	1.00

CRediT author statement

Pietro Morozzi: Conceptualization, Methodology, Formal analysis, Investigation, Writing - Original Draft, Visualization; **Barbara Ballarin:** Resources, Writing - Review & Editing; **Erika Brattich:** Writing - Review & Editing; **Franco Lucarelli:** Validation, Resources, Writing - Review & Editing; **Silvia Nava:** Validation, Resources, Writing - Review & Editing; **Pedro J. Gómez-Cascales:** Investigation; **Jose A. G. Orza:** Software, Formal analysis, Resources, Writing - Review & Editing, Supervision, Project administration, Funding acquisition; **Laura Tositti:** Conceptualization, Writing - Review & Editing, Supervision

Declaration of interests

☒ The authors declare that they have no known competing financial interests or personal relationships that could have appeared to influence the work reported in this paper.

☐The authors declare the following financial interests/personal relationships which may be considered as potential competing interests: